Analysis of a Nonconvective Mesoscale Windstorm and Wildfire Outbreak in Kansas on 15 December 2021

THOMAS J. GALARNEAU JR.[a] AND MICHELLE R. SPENCER[b,c,a]

[a] *NOAA/OAR National Severe Storms Laboratory, Norman, Oklahoma*
[b] *Cooperative Institute for Severe and High-Impact Weather Research and Operations, The University of Oklahoma, Norman, Oklahoma*
[c] *School of Meteorology, The University of Oklahoma, Norman, Oklahoma*

(Manuscript received 29 September 2024, in final form 14 December 2024, accepted 16 January 2025)

ABSTRACT: A rapidly deepening extratropical cyclone moved across the central Great Plains on 15 December 2021 and resulted in simultaneous extreme weather events. A derecho developed at the cold front and moved from the eastern half of Kansas to Wisconsin. Simultaneously, a nonconvective mesoscale windstorm occurred on the southwest side of the cyclone and moved from western to central Kansas and is the focus of this study. The windstorm downed power lines and triggered a wildfire outbreak covering over 160 000 ac (650 km^2) resulting in two fatalities, several injuries, and the loss of hundreds of cattle. Surface wind gusts exceeded 50 kt (26 m s^{-1}) over a large area in western Kansas with a peak gust of 87 kt (45 m s^{-1}) observed at Russell, Kansas, on the southeast flank of the largest wildfire in the region. The extratropical cyclone resembled the Shapiro–Keyser conceptual model with the mesoscale windstorm focused near the cloud head and southern tip of the bent-back front southwest of the cyclone center. The near-surface wind speeds were highest where three airstreams—one along the bent-back front and the other two at higher altitudes to the west of the cyclone—descended and accelerated in a higher horizontal pressure gradient region near the tip of the bent-back front and cloud head. While the nonconvective mesoscale windstorm did not meet the exact definition of a sting jet, it exhibited many of the same characteristics and physical mechanisms that drive sting jets with oceanic Shapiro–Keyser cyclones.

KEYWORDS: Fronts; Mesoscale processes; Extratropical cyclones; Extreme events; Wildfires; Wind

1. Introduction

Simultaneous extreme weather events occurred in the central Great Plains on 15 December 2021 in conjunction with a rapidly deepening extratropical cyclone. A serial derecho (Johns and Hirt 1987; Corfidi et al. 2016) developed along the cyclone's cold front in central Kansas at 1930 UTC and rapidly moved northeast reaching central Wisconsin by 0400 UTC 16 December, resulting in five fatalities and $1.8 billion in damage (NOAA 2024). The derecho was linked to 648 wind damage reports, including 170 with significant wind over 65 kt (33 m s^{-1}), and a record outbreak of 167 tornadoes, 39 of which were significant with an EF2 or higher rating on the enhanced Fujita scale (Fujita 1981; WSEC 2006). In the wake of the derecho, a separate nonconvective mesoscale windstorm occurred in western and north-central Kansas on the southwest side of the deepening cyclone near the southern end of the cloud head (Fig. 1). In addition to near the cloud head, nonconvective strong winds occurred farther south in Kansas, northwest Texas, and Oklahoma as evident from the dust plumes on visible satellite imagery at 2000 and 2100 UTC (Figs. 1a,b). Wildfires were ongoing in the Texas and Oklahoma Panhandles, and an outbreak[1] of wildfires developed in north-central Kansas by 2200 UTC and was clearly evident in the 2246 UTC visible satellite imagery as the cloud head evaporated (Figs. 1c,d).

The wildfire outbreak in north-central Kansas was linked to the nonconvective mesoscale windstorm which toppled power lines and sparked grass fires that spread amid near-surface winds over 50 kt (26 m s^{-1}) (Kite 2021). Conditions in north-central Kansas prior to the fires, while not in drought, were abnormally dry (Fig. 2a). From October through December 2021 observations at Russell, Kansas (RSL), located about 10 km south of the largest fire, showed no rainfall reported from 4 November until the wildfire outbreak on 15 December (Fig. 2b). As a result of the dry grasses and strong winds, the fires rapidly expanded east, burning over 160 000 ac (650 km^2) and leading to two fatalities, several injuries, and the loss of hundreds of cattle. While the derecho, nonconvective mesoscale windstorm, and wildfire outbreak are all worthy of detailed study due to their significant socioeconomic impacts, this study will focus on the nonconvective mesoscale windstorm and subsequent wildfires. Specifically, we will use observations and a convection-allowing numerical simulation to document the life cycle of the windstorm and the environment in which it occurred and to investigate the physical processes responsible for the damaging winds.

Supplemental information related to this paper is available at the Journals Online website: https://doi.org/10.1175/WAF-D-24-0195.s1.

Corresponding author: Thomas J. Galarneau, thomas.galarneau@noaa.gov

[1] A wildfire outbreak is defined by Lindley et al. (2014) as the "nearly simultaneous ignition and spread of 10 or more wind-driven fires spatially and temporally close to the passage of mid-latitude cyclones." At total of 54 wildfires ignited across 34 counties in Kansas on 15 Dec 2021 (State of Kansas 2023; Kansas Forest Service 2021).

DOI: 10.1175/WAF-D-24-0195.1

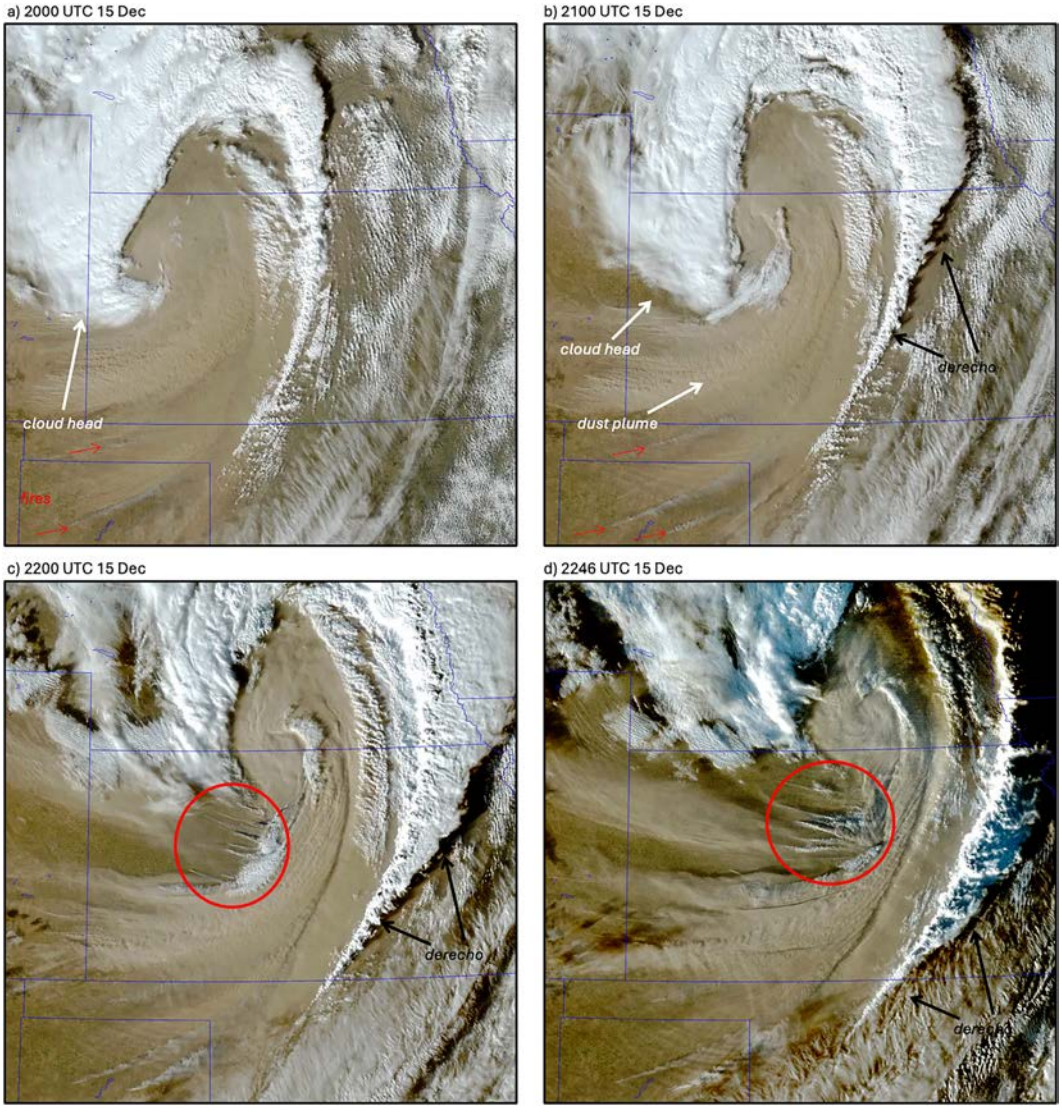

FIG. 1. *GOES-16* ABI true color visible satellite imagery at (a) 2000, (b) 2100, (c) 2200, and (d) 2246 UTC 15 Dec 2021. Selected active fires are marked in red arrows and an unfilled red circle. The cloud head and dust plume are labeled with a white arrow and derecho with a black arrow. Satellite image is from CIMSS (https://cimss.ssec.wisc.edu/satellite-blog/images/2021/12/211215_goes16_trueColorRGB_Plains_blowing_dust_anim.gif).

a. Background on nonconvective winds in extratropical cyclones

Nonconvective strong winds are a common occurrence in the United States and pose a significant hazard to life and property (Knox et al. 2011). The number of fatalities for wind-related hazards in the United States associated with nonconvective strong winds is similar to those associated with thunderstorm winds, which are second to tornadoes for 1980–2005 (Ashley and Black 2008). For nonconvective winds, over ¾ of the fatalities are linked to strong winds associated with extratropical cyclones. Nonconvective strong winds in extratropical cyclones have been linked to, for example, mesoscale gravity waves (e.g., Ruppert and Bosart 2014), terrain-influenced windstorms (e.g., Durran 1990), tropopause folds behind the cold front (e.g., Knox et al. 2011), the warm and cold conveyor belt airstreams (e.g., Carlson 1980; Grønås 1995; Brâncuş et al. 2019), and the sting jet airstream (e.g., Browning 2004; Schultz and Browning 2017; Clark and Gray 2018, for a review). Sting jets produce the most damaging nonconvective winds within extratropical cyclones and were first identified as a mesoscale region of particularly strong winds between the dry slot and the leading edge of the cold conveyor belt in Browning's (2004) reanalysis of the Great Storm of 16 October 1987 (Clark and Gray 2018).

The sting jet is defined as a coherent airflow above the cold conveyor belt that descends from the midtroposphere inside the cloud head of rapidly deepening Shapiro–Keyser cyclones (Shapiro and Keyser 1990, their Fig. 10.27) and reaches the

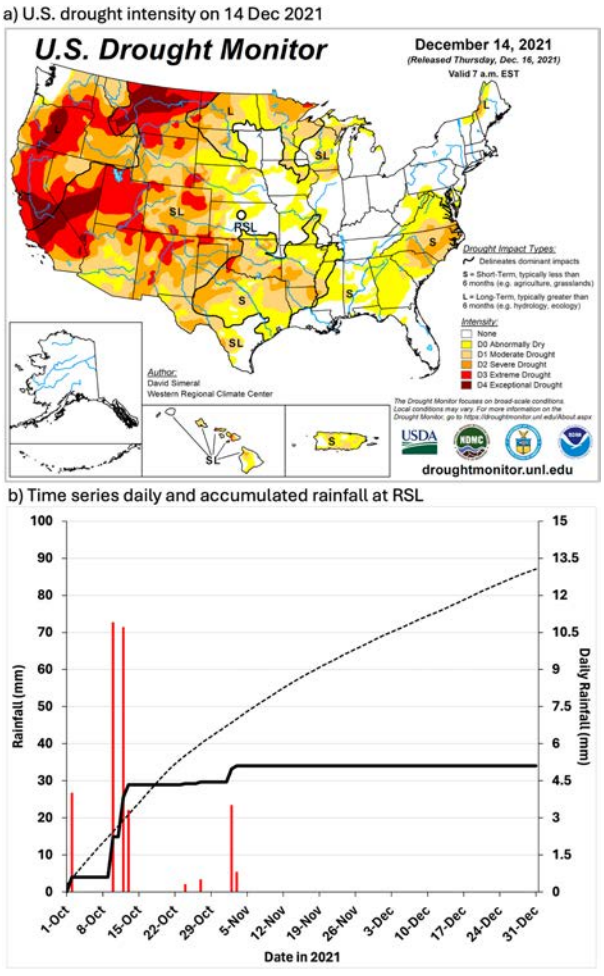

FIG. 2. (a) U.S. drought intensity (shaded according to the category D0–D4) on 14 Dec 2021. Image is available online (https://droughtmonitor.unl.edu/). (b) Time series of daily rainfall (red bars; mm; right *y* axis), accumulated rainfall (black line; mm; left *y* axis), and climatological accumulated rainfall (dashed line; mm; left *y* axis) at RSL on 1 Oct–31 Dec 2021.

top of the planetary boundary layer (PBL) ahead of the cold conveyor belt (Clark and Gray 2018, their Fig. 8). Multiple proposed mechanisms may be important to sting jet formation. Mesoscale descent associated with frontolysis near the tip of the bent-back front has been linked to the descent of the sting jet airstream (e.g., Schultz and Sienkiewicz 2013; Schultz and Browning 2017). The flow accelerates as the air moves into a region with a higher along-flow pressure gradient (e.g., Slater et al. 2015, 2017). Acceleration of the descending sting jet airstream has also been linked to the release of conditional symmetric instability (CSI; e.g., Gray et al. 2011), potential symmetric instability (PSI; e.g., Smart and Browning 2014), symmetric instability (SI) and inertial instability (II; e.g., Baker et al. 2014), and evaporative cooling in the cloud head (e.g., Clark et al. 2005).

Sting jets have been documented in about $\frac{1}{3}$ of all cyclones and nearly half of all rapidly deepening cyclones in the North Atlantic basin for 1979–2012 (e.g., Hart et al. 2017; Martínez-Alvarado et al. 2012). They occur preferentially in the western North Atlantic in the time-mean confluent upper-level jet entrance region where Shapiro–Keyser cyclones occur most frequently but have also been documented in western Europe and the Mediterranean Sea (Schultz et al. 1998; Brâncuş et al. 2019; Hatzaki et al. 2023). For example, sting jets are responsible for 21% of daily maximum wind gusts in the United Kingdom and are the dominant drivers of high wind events in the British Isles (Earl et al. 2017; Hart et al. 2017). Until recently, sting jets have not been systematically documented in other parts of the world. Knox et al. (2011) hypothesized that sting jets with Shapiro–Keyser cyclones have occurred in the Great Lakes region. Mass and Dotson (2010) did not identify any sting jets in eastern North Pacific and northwestern U.S. cyclones, but Kitabatake (2008) documented extratropical transition events in the western North Pacific that resembled warm seclusion Shapiro–Keyser cyclones. It is possible that sting jets occurred with those transitioning cyclones. Gray et al. (2024) generated a reanalysis-based global climatology of sting jet conditions associated with extratropical cyclones based on the "sting jet precursor" diagnostic and found that sting jets likely occur in the North Pacific and Atlantic basins and across the Southern Hemisphere.

The global climatology of sting jet conditions by Gray et al. (2024) shows a local sting jet genesis maximum in the southern Great Plains that is connected with the larger maximum in the western North Atlantic. The authors are unaware of any detailed case study analysis of a Shapiro–Keyser cyclone and sting jet in the Great Plains. However, cyclones with near-surface wind maxima southwest of the cyclone center that resembled sting jets have been documented. One such event occurred on 25–26 December 2016 in conjunction with a deepening cyclone that produced a mesoscale wind swath from northeast Colorado through Nebraska and northern Kansas and into Minnesota (Kelley et al. 2019). While the mesoscale near-surface wind maximum resembled a sting jet as it originated in the midtroposphere and descended in the cloud head, it was not a true sting jet as the winds were associated with a mountain wave and downslope windstorm that was able to expand eastward on top of a stable layer behind an Arctic front. So, while mesoscale windstorms that resemble sting jets have been documented in the Great Plains, detailed analysis and diagnosis of true sting jets in the Great Plains have not yet appeared in the refereed literature.

b. Background on wildfires in the Great Plains

Wildfires are a common occurrence in the contiguous United States. Perhaps, the most well known and studied wildfires occur in the densely forested Intermountain West in conjunction with synoptic and mesoscale windstorms such as the Santa Anas and Sundowners in California (e.g., Sommers 1978; Burroughs 1987; Abatzoglou and Kolden 2013; Smith et al. 2018). For instance, wildfire occurrences have been linked to enhanced Santa Ana winds that were driven by near-surface high pressure systems that set up in the Intermountain West in response to a Rossby wave train triggered

by the extratropical transition of tropical cyclones in the west Pacific (e.g., Bosart et al. 2017; Stuivenvolt-Allen et al. 2021; Stuivenvolt-Allen and Wang 2023). Wildfires are also a common occurrence in grassland biomes throughout the world, such as the Great Plains. The central Great Plains currently experience a bimodal wildfire season, with peaks in the early spring and fall when dry and windy conditions coincide with dormant and cured fuels (NWCG 2022). While there were reduced wildfires in the Great Plains in the twentieth century, the last 20 years have shown increases in the number of large wildfires, total area burned, and annual probability of wildfire occurrence (Donovan et al. 2017).

Megafires are defined as fires that burn over 100 000 ac (400 km^2) and have also shown an increasing trend globally (Lindley et al. 2019). In the Great Plains, megafires occur primarily in spring and occur preferentially during dry periods that follow wet periods and enhanced vegetation growth (see also Pyne 2017). The synoptic-scale weather patterns that favor megafires in the southern Great Plains include a progressive negatively tilted trough at 500 hPa moving through Colorado into Nebraska with attendant strong winds in New Mexico and Texas and into Kansas, an extratropical cyclone over Kansas, and a low-level thermal ridge in Texas and Oklahoma (Lindley et al. 2017, 2019). The wildfire outbreak on 15 December 2021 is classified as a megafire, with over 160 000 ac burned. We will show that the fires developed in association with strong winds on the south side of a deepening extratropical cyclone ahead of a negatively tilted trough, somewhat similar to the synoptic flow pattern of previous megafires in the Great Plains.

c. Science objectives

The nonconvective mesoscale windstorm and wildfire outbreak in Kansas in the wake of a serial derecho on 15 December 2021 represent simultaneous, or compounding (Zscheischler et al. 2020), extreme weather events with notable socioeconomic impacts. This study will focus on the mesoscale windstorm. We aim to examine the overall life cycle of the mesoscale windstorm from a multiscale perspective and determine the physical processes that contributed to the surface wind maximum. Given the at least superficial similarity 1) of the cyclone structure with Shapiro–Keyser cyclones and 2) between the near-surface wind maximum and sting jets, we will compare and contrast the present case with more typical sting jets documented with oceanic Shapiro–Keyser cyclones. Observations, National Centers for Environmental Prediction (NCEP) operational model analyses and forecasts, and a convection-allowing numerical simulation will be used to address the goals of this study.

d. Organization

The remainder of the paper is structured as follows. Section 2 presents the datasets used and methods employed. Section 3 uses observations, operational model analyses, and forecasts to provide a multiscale synoptic and mesoscale analysis of the cyclone and the nonconvective mesoscale wind maximum. Section 4 presents the results from a convection-allowing numerical simulation used to diagnose the nonconvective mesoscale wind maximum, and section 5 compares the 15 December 2021 event to sting jets documented in oceanic Shapiro–Keyser cyclones. Section 6 provides the conclusions.

2. Data and methods

This study uses a combination of observations and numerical model datasets. Storm damage information was obtained from the National Oceanic and Atmospheric Administration (NOAA)/National Centers for Environmental Information (NCEI) Storm Events Database, version 3.1 (NOAA 2024). Automated Surface Observing System (ASOS) observations were retrieved from NOAA/NCEI, and precipitation data at RSL were obtained from the NOAA/National Weather Service (NWS) Climate Prediction Center. *GOES-16* Advanced Baseline Imager (ABI) true-color satellite imagery was obtained from the Cooperative Institute for Meteorological Satellite Studies satellite blog and shortwave window infrared imagery from the NOAA/NWS weather forecast office in Wichita, Kansas. The operational Global Forecast System (GFS) model pressure-level data on 0.5° latitude–longitude grid spacing were retrieved from NOAA/NCEI and the operational High-Resolution Ensemble Forecast, version 3 (HREF), from the NOAA/NWS Storm Prediction Center (SPC).

A convection-allowing numerical simulation was generated using the Advanced Research version 3.9 of the Weather Research and Forecasting (ARW; Skamarock et al. 2008) Model. The simulation is a single domain shown in Fig. 3a and is initialized at 1200 UTC 15 December 2021 using the fifth major global reanalysis produced by the European Centre for Medium-Range Weather Forecasts (ERA5; Hersbach et al. 2020) as initial and hourly lateral boundary conditions. The domain is configured with 601 × 601 grid points at 3-km horizontal grid spacing and 51 vertical levels up to 20 hPa. The physics options are consistent with the NOAA National Severe Storms Laboratory Warn-on-Forecast System (WoFS; Heinselman et al. 2024) and are as follows: no cumulus parameterization, NSSL two-moment microphysics (Mansell et al. 2010), Rapid Update Cycle land surface model (Smirnova et al. 2016), Yonsei University (YSU; Hong et al. 2006) PBL scheme, Dudhia (1989) shortwave and RRTM longwave radiation called every 5 min, second-order diffusion for turbulence and mixing, and horizontal Smagorinsky first-order closure for eddy viscosity.

To diagnose the forcing for vertical motion near the nonconvective mesoscale windstorm, the Miller (1948) two-dimensional frontogenesis is computed as

$$F = \frac{1}{|\nabla\theta|}\left[-\frac{\partial\theta}{\partial x}\left(\frac{\partial u}{\partial x}\frac{\partial\theta}{\partial x}+\frac{\partial v}{\partial x}\frac{\partial\theta}{\partial y}\right)-\frac{\partial\theta}{\partial y}\left(\frac{\partial u}{\partial y}\frac{\partial\theta}{\partial x}+\frac{\partial v}{\partial y}\frac{\partial\theta}{\partial y}\right)\right], \quad (1)$$

where F is frontogenesis, ∇ is the gradient operator on a pressure surface, $\partial/\partial x$ and $\partial/\partial y$ are the derivatives on a pressure surface, θ is the potential temperature, u is the zonal wind component, and v is the meridional wind component. The Miller (1948) formulation is equivalent to Petterssen's (1936) frontogenesis function, where frontogenesis is driven by

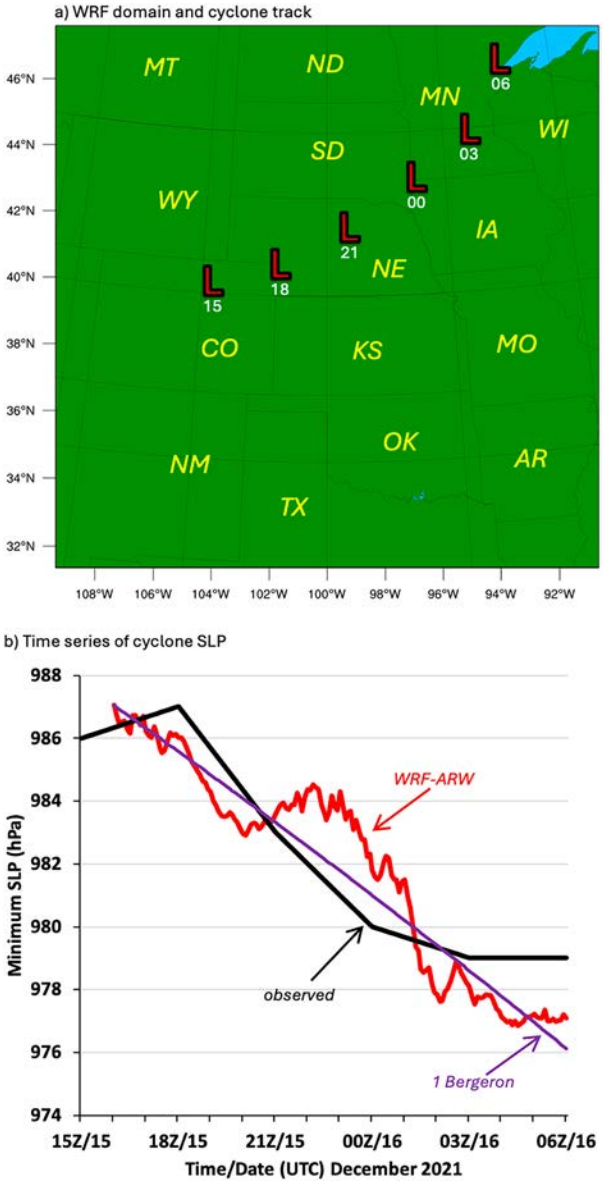

FIG. 3. (a) ARW model domain extent and simulated 3-h positions of the surface cyclone low pressure center (red-filled black L; hour in white) from 1500 UTC 15 Dec (3 h) to 0600 UTC 16 Dec 2021 (18 h). (b) Time series of cyclone minimum sea level pressure (hPa) derived from observations (black) and ARW (red). The predicted sea level pressure (hPa) from the initial ARW value at 1600 UTC using the deepening rate of 1 Bergeron, as defined by Sanders and Gyakum (1980), is shown in purple.

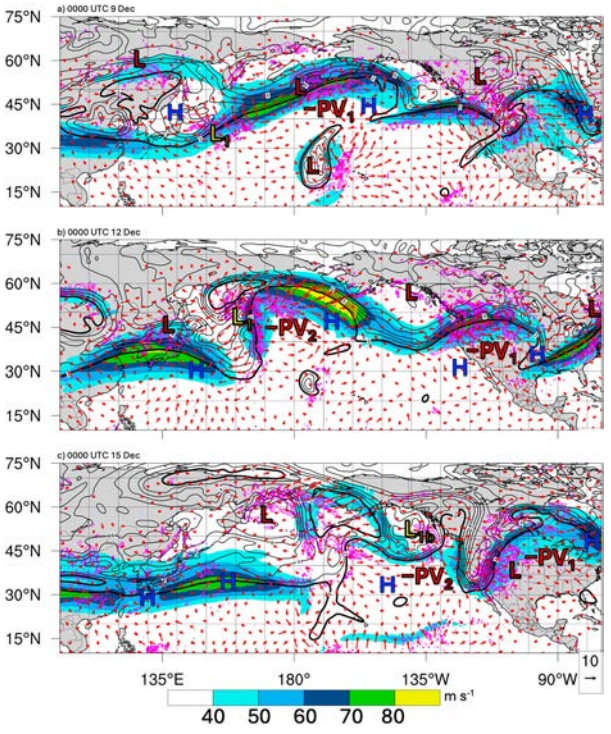

FIG. 4. GFS analysis 300–200-hPa layer-mean PV (black contours every 1 PVU starting at 2 PVU; 1 PVU = 10^6 K kg^{-1} m^2 s^{-1}), wind speed (shaded; m s^{-1}), 600–400-hPa layer-mean ascent (magenta contours every 0.3 Pa s^{-1} starting at −0.3 Pa s^{-1}), and irrotational wind (arrows; m s^{-1}) at 0000 UTC (a) 9 Dec, (b) 12 Dec, and (c) 15 Dec 2021. Surface high and low pressure systems are marked H and L, respectively. Key surface cyclogenesis event in the North Pacific is marked by a yellow-filled black L. Upper-level negative PV anomalies are labeled.

confluence and horizontal shear of the horizontal full wind (Keyser et al. 1988). The effects of tilting and diabatic heating are neglected here. Frontogenesis has been used to diagnose vertical motion in numerous studies across a wide array of weather systems, such as extreme rainstorms (e.g., Galarneau and Zeng 2020), precipitation bands in extratropical cyclones (e.g., Kenyon et al. 2020), and sting jets in oceanic cyclones (e.g., Schultz and Sienkiewicz 2013). Here, the wind and temperature fields are sampled every fourth grid point and are smoothed to remove small-scale features (<50 km) prior to computing frontogenesis. For the Lagrangian analysis, air parcel trajectories were generated from the 5-min ARW output using the Read/Interpolate/Plot, version 4.7, software package. To compute trajectories, the three-dimensional velocity data available every 5 min were linearly interpolated to a 50-s trajectory time step.

3. Results: Synoptic and mesoscale analysis

The aims of this section are to establish the multiscale evolution of the synoptic-scale flow that led to robust extratropical cyclogenesis in eastern Colorado and document the structure and evolution of the cyclone and attendant surface wind maximum.

a. Synoptic-scale flow

The synoptic-scale flow pattern in the North Pacific and North America was characterized by a quasi-zonal jet stream with a low-amplitude ridge, marked by a region of negative potential vorticity (PV) labeled $-PV_1$, in the central Pacific with flanking troughs in the western and eastern Pacific at 0000 UTC 9 December (Fig. 4a). A surface low pressure

system (labeled L_1) was located near 35°N, 145°E in the equatorward jet entrance region of the 250-hPa North Pacific jet stream. The low pressure system underwent explosive cyclogenesis and was located near 50°N, 160°E by 0000 UTC 12 December (Fig. 4b). Divergent outflow at 250 hPa developed in conjunction with a large area of precipitation (inferred from a region of 600–400-hPa layer-mean ascent) along the warm front extending east of the cyclone and on the north side of an upper-level ridge ($-PV_2$). Downstream amplification occurred in response to the divergent outflow increasing the PV gradient and strengthening the 250-hPa jet in the north-central Pacific. Secondary cyclogenesis developed along the primary cyclone's warm front and moved east to the Gulf of Alaska by 0000 UTC 15 December (labeled L_{1b}) (Fig. 4c). The downstream amplification resulted in a meridionally elongated trough in the western United States. A surface lee trough developed in eastern Colorado in advance of the upper-level trough and then rapidly deepened as an extratropical cyclone as it moved east away from the Rockies after 1500 UTC (Fig. 3b). The deepening period of the cyclone at a rate near 1 Bergeron, defined by Sanders and Gyakum (1980) as the cyclone deepening rate in 24 h normalized by the latitude relative to 60°N as $\sin(\phi)/\sin(60°)$, was short lived compared to oceanic "bomb" cyclones and ended by 0000 UTC 16 December. Similar to synoptic patterns associated with wildfires in other parts of the United States (e.g., Bosart et al. 2017), the North American synoptic pattern for the nonconvective mesoscale windstorm and wildfires on 15 December 2021 was linked to rapid cyclogenesis in the western North Pacific and downstream amplification.

The HREFv3 forecast initialized at 1200 UTC 15 December showed a synoptic-scale flow pattern in the central Great Plains that resembled the megafire pattern introduced by Lindley et al. (2019) and examined further by Lindley et al. (2023). A negatively tilted trough at 500 hPa was located in northeast Colorado with a curved jet streak over 100 kt (51 m s^{-1}) in southwest Kansas at 1800 UTC (Fig. 5a). A deepening surface cyclone was located in southwest Nebraska with a cold front extending southward into western Kansas and Oklahoma (Fig. 5b). The 500-hPa trough and surface cyclone moved northeastward through Nebraska, with the 500-hPa jet streak intensifying to over 130 kt (67 m s^{-1}) and a surface dry slot surging eastward to central Kansas and northward to near the cyclone center by 2100 UTC (Figs. 5c,d). The dry slot region in western Kansas that overlapped with the sea level pressure gradient south of the cyclone center aligned with the day-1 fire weather outlook by SPC at 1700 UTC. The outlook highlighted critical fire weather conditions from eastern Colorado and New Mexico to southeast Nebraska, including an extreme fire weather risk from the Texas Panhandle to north-central Kansas, due to the potential for a fire weather outbreak with the strong near-surface winds and low relative humidity values. Differing from the typical megafire pattern identified by Lindley et al. (2019), the fire weather conditions were located west of the warm sector and low-level thermal ridge. By 0000 UTC 16 December, the 500-hPa trough and surface cyclone had moved northeastward to northeastern Nebraska and eastern South Dakota (Figs. 5e,f).

b. *Cyclone structure and surface winds*

A manual surface analysis of the deepening extratropical cyclone at 2100 UTC 15 December reveals structural similarity to stage III of the Shapiro–Keyser extratropical cyclone model [Fig. 6; compare to Fig. 10.27 in Shapiro and Keyser (1990)]. A frontal T-bone at the intersection of the cold and warm fronts east of the cyclone center, a developing warm seclusion at the cyclone center, and a bent-back front southwest of the cyclone center are all evident in the cyclone structure. The bent-back front formed as the cyclone developed and moved northeast along an Arctic front that was moving southward in the lee of the Rockies. The Arctic and bent-back front formation did not occur as seen in oceanic Shapiro–Keyser cyclones but more like what was seen in the Great Plains cyclone on 25–26 December 2016 (Kelley et al. 2019, their Fig. 2). A band of precipitation was associated with the cloud head and sea level pressure trough located along the bent-back front in northwest Kansas (Figs. 1 and 6). The leading edge of the dry slot was located just west of the derecho and cold front and south of the cyclone center, with surface dewpoints decreasing from near 50°F (10°C) to below 10°F (−12°C) within the dry slot. Numerous wind gusts over 50 kt were observed within the dry slot across western Kansas.

The shortwave infrared satellite imagery shows the derecho in central Kansas and the cyclone cloud head along the bent-back front on the Kansas–Colorado border at 2000 UTC 15 December (Fig. 7a). Peak hourly wind gusts exceeded 50 kt over much of Kansas in conjunction with the derecho, southerly flow in the warm sector, the dry slot, and the cloud head. The hourly and special METARs for stations impacted by the cloud head are provided in the online supplemental material. As the systems moved eastward, the strongest observed surface wind gusts over 70 kt (36 m s^{-1}) were associated with the derecho and cloud head (Figs. 7b–d). The highest wind gust reported was 87 kt (45 m s^{-1}) at RSL with the passage of the cloud head. As the cloud head moved eastward producing damaging surface winds, it evaporated much like the cloud head associated with oceanic Shapiro–Keyser cyclones that produced sting jets (e.g., Browning 2004). The meteograms derived from 1-min ASOS at two stations near the cloud head [Goodland, Kansas (GDL), and RSL] and one station in the dry slot [Dodge City, Kansas (DDC)] show an extended period of high winds above 50 kt with the passage of the cyclone to the north (Fig. 8). The dry slot was most pronounced at RSL and DDC with winds gusting over 60 kt (31 m s^{-1}). However, the highest wind gusts occurred during the passage of the cloud head with a peak gust of 70 kt at GLD and 87 kt at RSL (Figs. 8a,b). The wind peaks occurred while the 2 m AGL dewpoint was rapidly increasing as the cloud head approached. The highest wind gusts at DDC, farther south of the cloud head, occurred with the approach of the dry slot (Fig. 8c). The dark regions on the shortwave infrared satellite imagery indicate where fires are active (Fig. 7). Most of the fires in Kansas, including the largest fire that occurred just northwest of RSL, began during the passage of the cloud head and its attendant

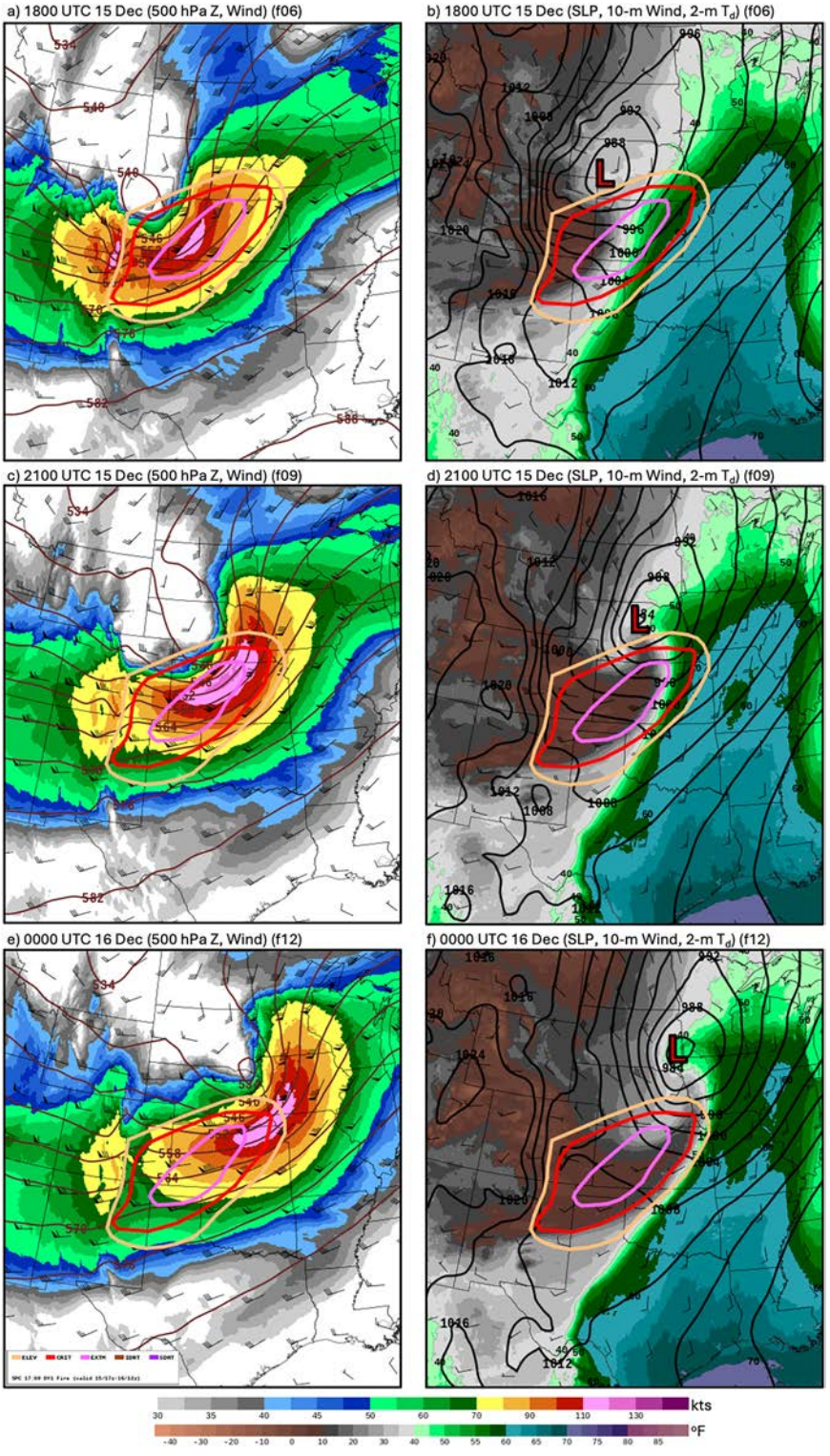

FIG. 5. HREFv3 ensemble mean forecast 500-hPa geopotential height (brown contours every 6 dam), wind speed (shaded; kt), and vector wind (standard barbs; kt) at (a) 1800 UTC 15 Dec, (c) 2100 UTC 15 Dec, and (e) 0000 UTC 16 Dec 2021. (b),(d),(f) As in (a), (c), and (e), but showing sea level pressure (black contours every 4 hPa), 10-m vector wind (standard barbs; kt), and 2-m dewpoint (shaded; °F). HREFv3 forecast is initialized at 1200 UTC 15 Dec. The SPC day-1 fire weather outlook is overlaid according to the key on the lower left of (e). Images and information on model configuration are available online (https://www.spc.noaa.gov/exper/href/).

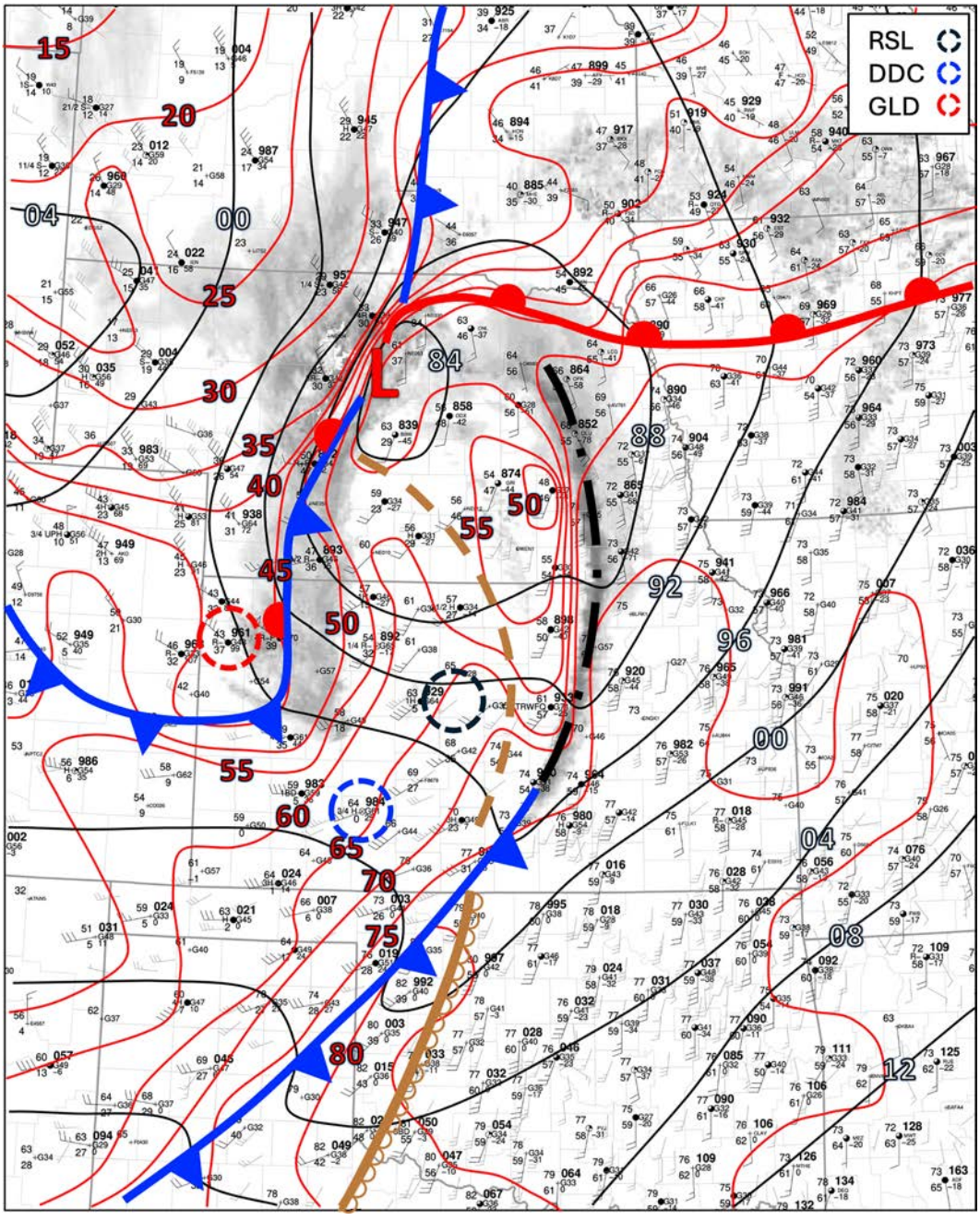

FIG. 6. Manual surface analysis at 2100 UTC 15 Dec 2021 of sea level pressure (black contours every 4 hPa) and temperature (red contours every 5°F) overlaid on radar base reflectivity mosaic (shaded in gray). Cold (blue), warm (red), and stationary fronts (blue and red), dryline (brown solid), and derecho (black dash–dotted) are labeled using conventional symbols. The brown-dashed line segment marks the approximate leading edge of the dry slot (dewpoints $< \sim 30$°F). The cyclone low pressure center is marked by the red-filled L. The locations of ASOS stations at RSL, GLD, and DDC are marked according to the key in the upper-right inset. The base map is from the NCEP SPC archive (https://www.spc.noaa.gov/exper/surfaceMaps/).

mesoscale region of high winds (not the dry slot winds) that followed the extremely dry conditions in the dry slot the preceding hour and abnormally dry conditions the preceding weeks (see also Fig. 2).

4. Results: Nonconvective mesoscale wind maximum

The aim of this section is to use a convection-allowing ARW simulation to examine the structure and evolution of the nonconvective mesoscale windstorm on the southwest

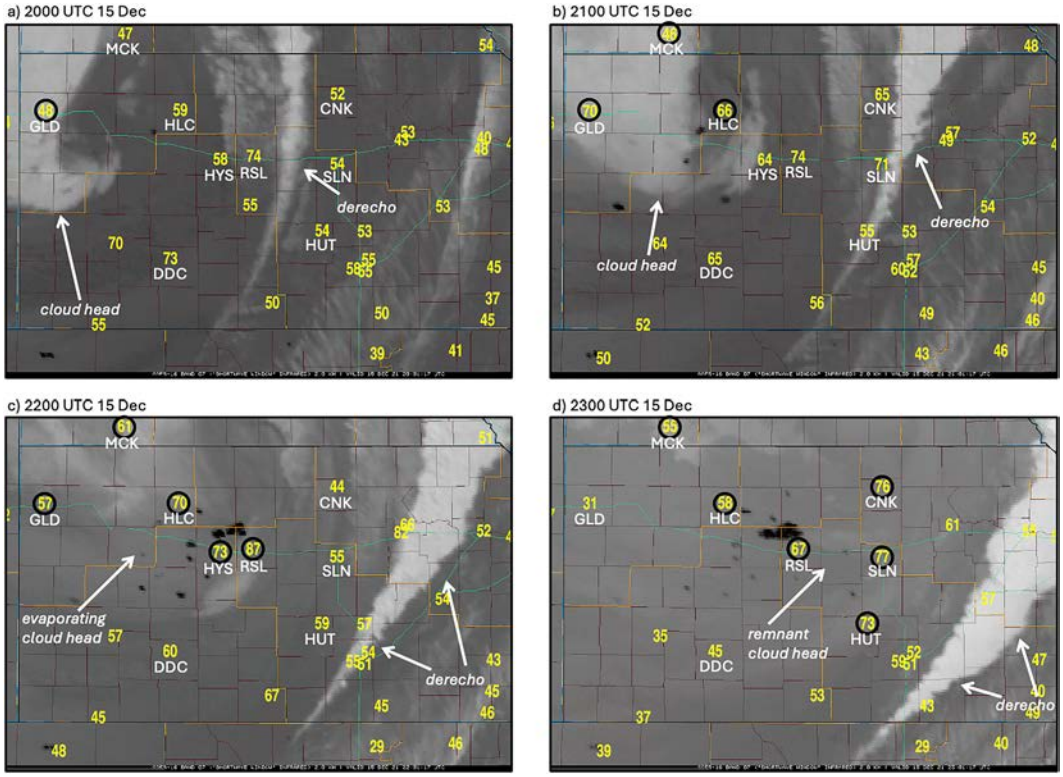

FIG. 7. *GOES-16* shortwave window infrared satellite imagery at (a) 2000, (b) 2100, (c) 2200, and (d) 2300 UTC 15 Dec 2021. The cloud head and derecho are labeled with white arrows. Hourly maximum reported wind gusts over 25 kt (13 m s^{-1}) at selected ASOS are shown in yellow. High wind gusts associated with the passage of the cloud head are indicated by an unfilled black circle, and the hourly and special METAR observations for these stations are provided in the supplemental material. Satellite imagery is available online (https://www.weather.gov/ict/event_2021Dec15thWindFireSVR).

side of the deepening cyclone. Specifically, we investigate the physical mechanisms driving the high winds.

a. Overview of numerical simulation

The simulation was initialized at 1200 UTC 15 December prior to when surface cyclogenesis was underway in northeast Colorado (not shown). The cyclone position and intensity were consistent with the observed storm during cyclogenesis near 1500 UTC 15 December and thereafter through 0600 UTC 16 December (Figs. 3 and 9). By 1800 UTC, the simulated cyclone was positioned along the Colorado–Nebraska border and near the beginning of a period of brief rapid intensification at rates near 1 Bergeron, similar to oceanic bomb cyclones (Fig. 9a). A mesoscale sea level pressure trough and developing cloud head, as apparent from a region of maximum simulated reflectivity over 10 dB*Z*, extended southwest of the cyclone center in eastern Colorado. A region of precipitation that later became the derecho was located along the leading edge of the cold front in western Kansas. As the surface cyclone moved northeast through 2100 UTC, the structure resembled the observed system with a derecho developing along the cold front and a well-defined cloud head and mesoscale surface trough of low pressure on the southwest side of the cyclone (Figs. 9a–d). After 2100 UTC, the surface cyclone and derecho moved northeast toward Iowa and eastern Nebraska (Figs. 9e,f). The cloud head evaporated in north-central Kansas as the surface pressure trough weakened similar to the observed evolution (Figs. 1b,d, 7b,d, and 9d–f).

The structure of the cyclone at 2100 UTC, during the period of rapid deepening, resembled phase III of the Shapiro–Keyser cyclone model (Fig. 10a; compare with their Fig. 10.27). Similar to the cyclone structure depicted in observations and with phase III of the Shapiro–Keyser model, a frontal T-bone structure was apparent near the intersection point of the cold and warm fronts and a bent-back front extended southwest of the cyclone center and connected with the Arctic front. A warm seclusion near the cyclone center and behind the cold front was beginning to develop. The cloud head was located along the bent-back front (see also Fig. 9d). A mesoscale wind maximum with near-surface winds exceeding 33 m s^{-1} was located at the southern tip of the bent-back front, while slightly weaker winds under 30 m s^{-1} were found within the dry slot between the bent-back and cold fronts (Fig. 10b). The structural resemblance of the rapidly deepening cyclone to the Shapiro–Keyser cyclone model is important because it 1) shows a cyclone structure in the southern Great Plains that is typically found over the western side of ocean basins and 2) opens the possibility that the mesoscale wind maximum near the tip of the bent-back front was similar to oceanic sting jets.

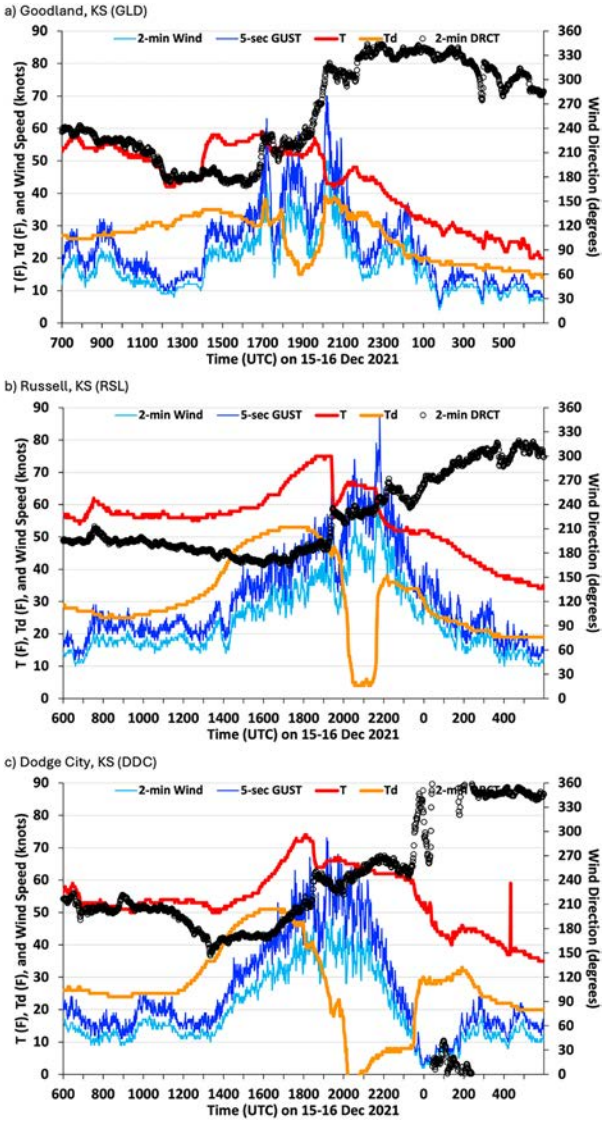

FIG. 8. Time series of 2 m AGL temperature (red line; °F; left *y* axis), dewpoint (orange line; °F; left *y* axis), 5-s wind gust (blue; kt; left *y* axis), 2-min wind speed (light blue; kt; left *y* axis), and 2-min wind direction (unfilled black circles, °; right *y* axis) at (a) GLD, (b) RSL, and (c) DDC for the time (UTC) shown on the *x* axis for 15–16 Dec 2021. These data are derived from the 1-min time resolution ASOS dataset.

b. *Evolution of vorticity and vertical structure of near-surface wind maximum*

The upper-level trough emerged in the High Plains just after 1500 UTC 15 December. At 1515 UTC, the core of the trough at 700 hPa was located in the western part of the Palmer Divide in eastern Colorado (Fig. 11a). A cyclonic shear zone was apparent north of the Palmer Divide at both 700 and 800 hPa, with bands of vertical vorticity (labeled "vorticity strip") located along the front range of the Rockies and the western flank of the 700-hPa trough (Figs. 11a,b). South of the Palmer Divide, a band of vertical vorticity was positioned at the leading edge of the westerly flow and Pacific cold front. This band eventually became the surface cold front in Kansas where the derecho developed later in the afternoon. As the trough moved east across and just northeast of the Palmer Divide by 1645 UTC, the strip of cyclonic vorticity at 700 hPa on the west side of the trough continued eastward and marked the leading edge of the westerly flow (Figs. 11c,e). Several individual vorticity banners at 800 hPa developed in the lee of the Palmer Divide in a region of cyclonic shear between the south-southwesterly flow east of the Palmer Divide and weaker flow to the north (Fig. 11d). The vorticity banners at 800 hPa merged with the vorticity strip along the leading edge of the westerly flow at 700 hPa as the synoptic-scale trough moved to the east (Fig. 11e). The elongated strip of cyclonic vorticity that developed in the lee of the Rockies and north of the Palmer Divide and on the western flank of the trough at the 700- and 800-hPa level became the bent-back front as the surface cyclone intensified and moved northeast into Nebraska.

By 1700 UTC, an arcing band of cyclonic vorticity at 800 hPa extended from near the Palmer Divide to northeast Colorado along the west flank of the surface low and the north flank of the core of the 500-hPa trough (Fig. 12a). Through 1900 UTC, the band of vorticity consolidated, became more north–south elongated, and the southern end closer to the core of the 500-hPa trough and attendant westerly flow began to cyclonically roll up (Figs. 12b,c). The roll up of the cyclonic vorticity strip coincided with a decrease in sea level pressure and a sharpening of the near-surface pressure trough at the southern tip of the bent-back front. Concurrently, the near-surface wind maximum increased to over 35 m s^{-1} through 2100 UTC as the system moved eastward across northwest Kansas (Figs. 12c–e). A similar evolution of vorticity and pressure decreases at the southern tip of the bent-back front was documented by Reed et al. (1994) in their adiabatic simulation of a rapidly deepening oceanic Shapiro–Keyser cyclone. By 2100 UTC, the vorticity roll up and southern tip of the bent-back front continued to move eastward with winds over 35 m s^{-1} before beginning to weaken likely due to increased vertical wind shear and deformation as the surface cyclone and 500-hPa trough moved away to the northeast (Fig. 12f).

The vertical structure of the near-surface wind maximum in west–east vertical cross sections at 1945 and 2100 UTC showed it occurred beneath the cloud head and west of the dry slot with maximum winds over 45 m s^{-1} near the 800-hPa level (Figs. 13a,c). The wind maximum was tilted in the vertical on both sides of the 800-hPa wind maxima, especially to the west where the strongest winds sloped upward to the top of the cool Arctic air mass west of the bent-back front. Farther west, mountain waves and a downslope windstorm were apparent in the lee of the Rockies with a region of dry air that extended eastward on the High Plains of Colorado. The west–east vertical cross section does not appear to indicate an elevated wind maximum that connects the downslope windstorm with the near-surface wind maximum at the tip of the bent-back front. However, the northwest–southeast vertical cross sections that are oriented farther north into the Arctic air mass show an elevated wind maximum that appears to show a

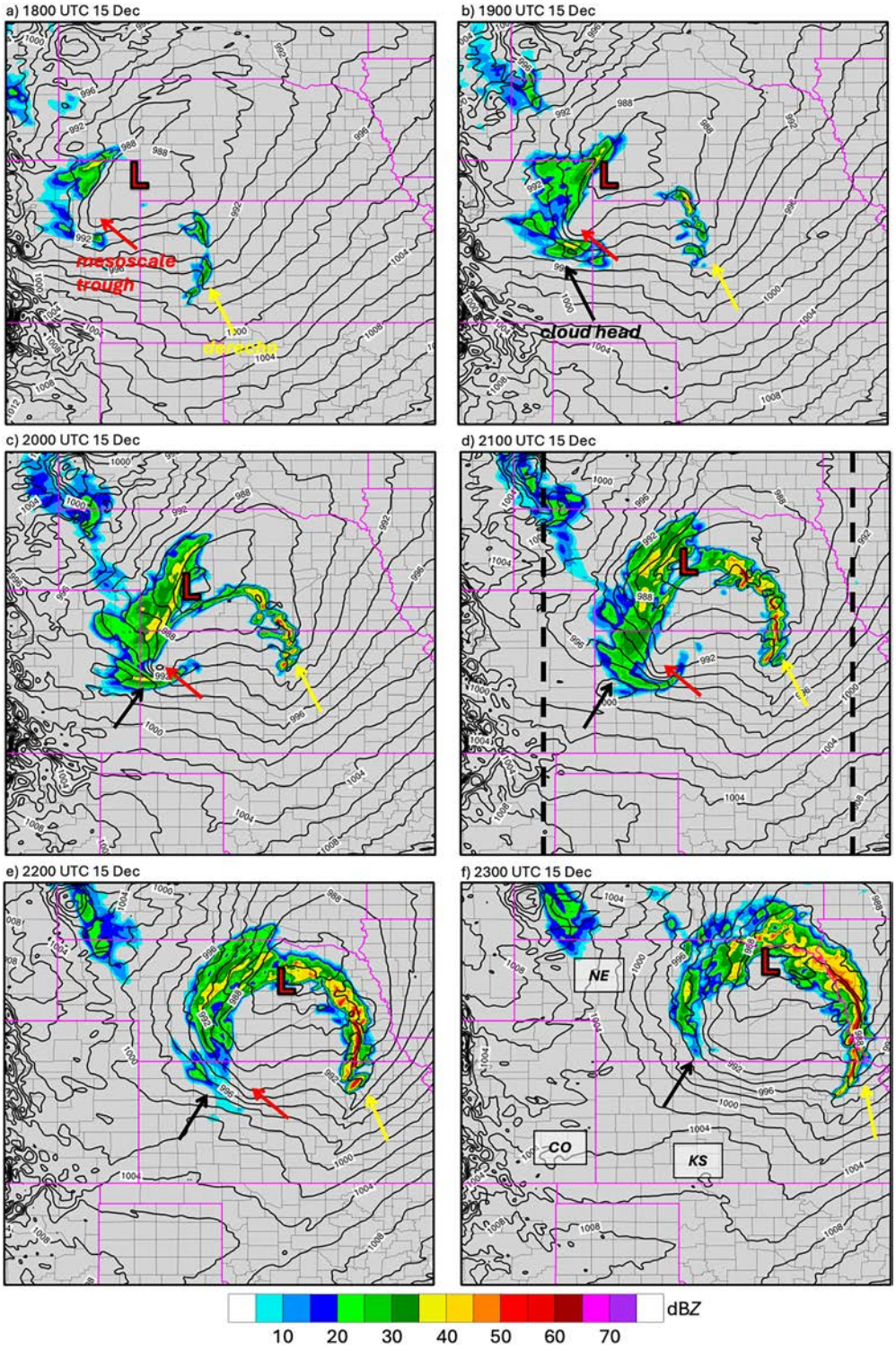

FIG. 9. ARW sea level pressure (black contours every 2 hPa) and 1-km reflectivity (shaded; dBZ) at (a) 1800 (6 h), (b) 1900 (7 h), (c) 2000 (8 h), (d) 2100 (9 h), (e) 2200 (10 h), and (f) 2300 UTC (11 h) 15 Dec 2021. The derecho (yellow arrow), cloud head (black arrow), and mesoscale trough at the tip of the bent-back front (red arrow) are labeled. The cyclone low pressure center is marked by the red-filled black L. The vertical dashed black line segments in (d) mark the west and east bounds of the maps shown in Fig. 10.

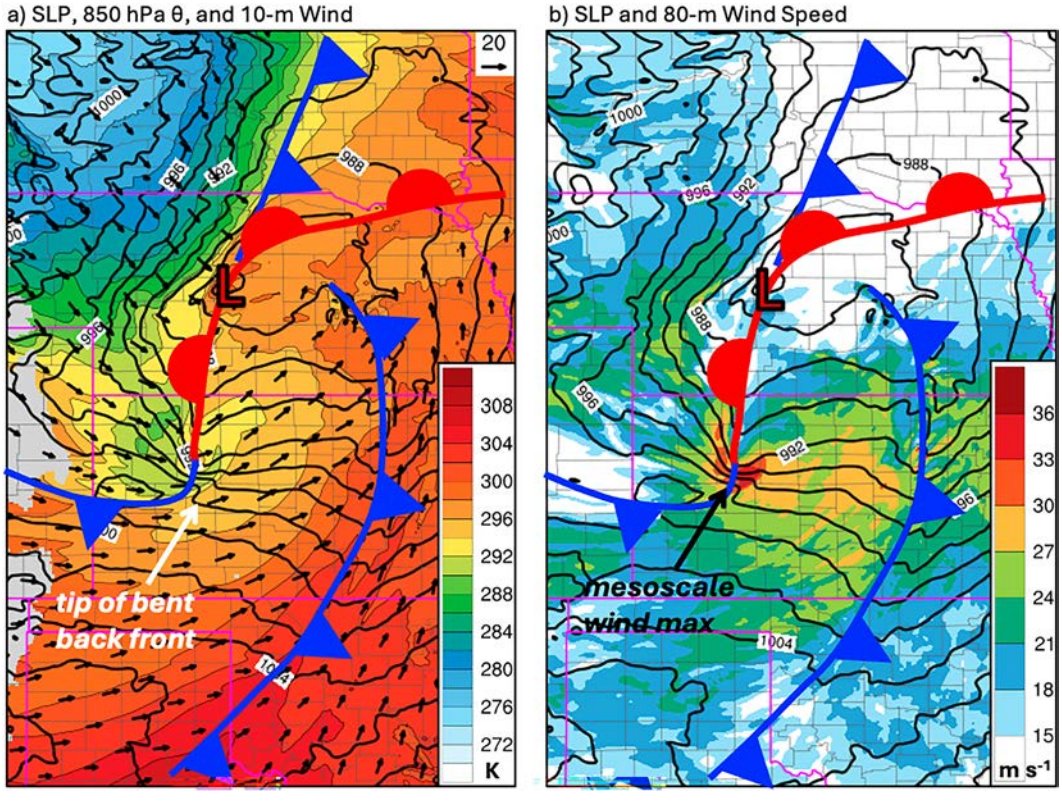

FIG. 10. ARW (a) sea level pressure (black contours every 2 hPa), 10 m AGL wind (arrows, m s^{-1}), and 850-hPa potential temperature (shaded; K), and (b) sea level pressure (black contours every 2 hPa) and 80 m AGL wind speed (shaded; m s^{-1}) at 2100 UTC (9 h) 15 Dec 2021. Surface fronts are marked using conventional symbols and are derived from interpretations based on the 2-m temperature (not shown). The cyclone low pressure center is marked by a red-filled black L. The tip of the bent-back front is marked by a white arrow in (a) and the mesoscale wind maximum is marked by a black arrow in (b).

connection to the mountain waves and downslope windstorm (Figs. 13b,d). A similar wind structure was documented in the 25–26 December 2016 windstorm and surface cyclone by Kelley et al. (2019, their Fig. 11). The vertical cross sections also show how the mesoscale wind maximum near the bent-back front is located closer to the ground in a region of reduced static stability (vertically oriented isentropes) near the bent-back front and the leading edge of the Arctic air mass (Fig. 13).

c. *Lagrangian cyclone–relative flow and wind accelerations*

The cyclone-relative airstreams at 1945 and 2100 UTC are determined by computing backward air parcel trajectories seeded at 825 and 875 hPa, respectively, at grid points near the southern end of the bent-back front where the wind speed exceeded 33 m s^{-1}. The near-surface wind maximum first reached 33 m s^{-1} as it entered western Kansas by 1945 UTC. The backward air parcel trajectories released at 1945 UTC and plotted at positions relative to the southern tip of the bent-back front in Fig. 14a revealed that the air at 825 hPa in the near-surface wind maximum was comprised of the 1) dry slot airstream originating from the southwest, 2) westerly flow airstream originating from the west and northwest above the Arctic air mass, and 3) bent-back airstream originating from the north along the bent-back front. All three airstreams descended from near 725 to 825 hPa in 3 h as they approached the near-surface wind maximum (Figs. 14a and 15a). Unlike the decreasing relative humidity during the descent of the dry slot airstream, the relative humidity increased as the westerly flow and bent-back airstreams moved through the cloud head during their descent (Fig. 15b). The dry slot airstream wind speed remained near 33 m s^{-1} during descent to lower altitudes (Fig. 15c). The westerly flow and bent-back airstreams accelerated as they descended, with increased acceleration of the wind speeds as the parcels moved through the cloud head and into the higher horizontal pressure gradient region near the tip of the bent-back front (Figs. 15c,d).

The backward air parcel trajectories seeded at 2100 UTC, when the near-surface wind maximum had its highest winds covering the largest area in west-central Kansas near where the wildfires were concentrated in observations, show similar characteristics of the three airstreams as for the trajectories seeded at 1945 UTC (Figs. 14b and 16). The westerly flow relative humidity was drier on average with a larger interquartile range for the trajectories seeded at 2100 UTC compared to earlier trajectories because some of the parcels moved through

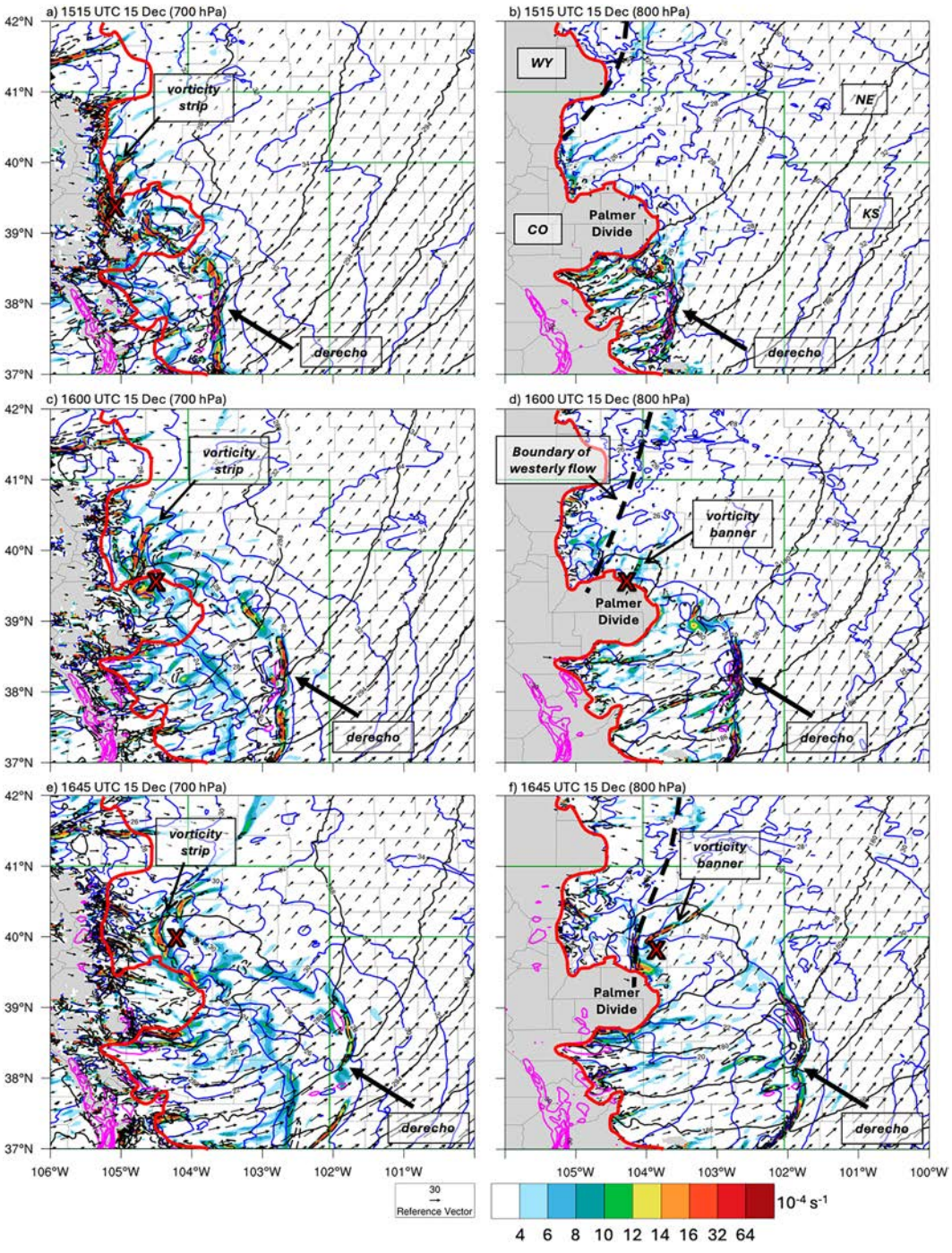

FIG. 11. ARW 700-hPa geopotential height (black contours every 3 dam), wind (arrows; m s^{-1}), potential temperature (blue contours every 2°C), relative vorticity (shaded; 10^{-4} s^{-1}), and resultant deformation (black dashed contours every 10×10^{-4} s^{-1} starting at 10×10^{-4} s^{-1}) at (a) 1515 (3.25 h), (c) 1600 (4 h), and (e) 1645 UTC (4.75 h) 15 Dec 2021. (b),(d),(f) As in (a), (c), and (e), but at the 800-hPa pressure level. Key vorticity features and the eventual derecho are labeled with a black arrow. The geopotential height minimum developing over and east of the Palmer Divide in eastern Colorado is marked with a red-filled black x. The leading edge of westerly flow at 800-hPa north of the Palmer Divide is marked by a black dashed line segment. The location where the 800-hPa pressure level intersects ground level is marked by the red contour in all panels.

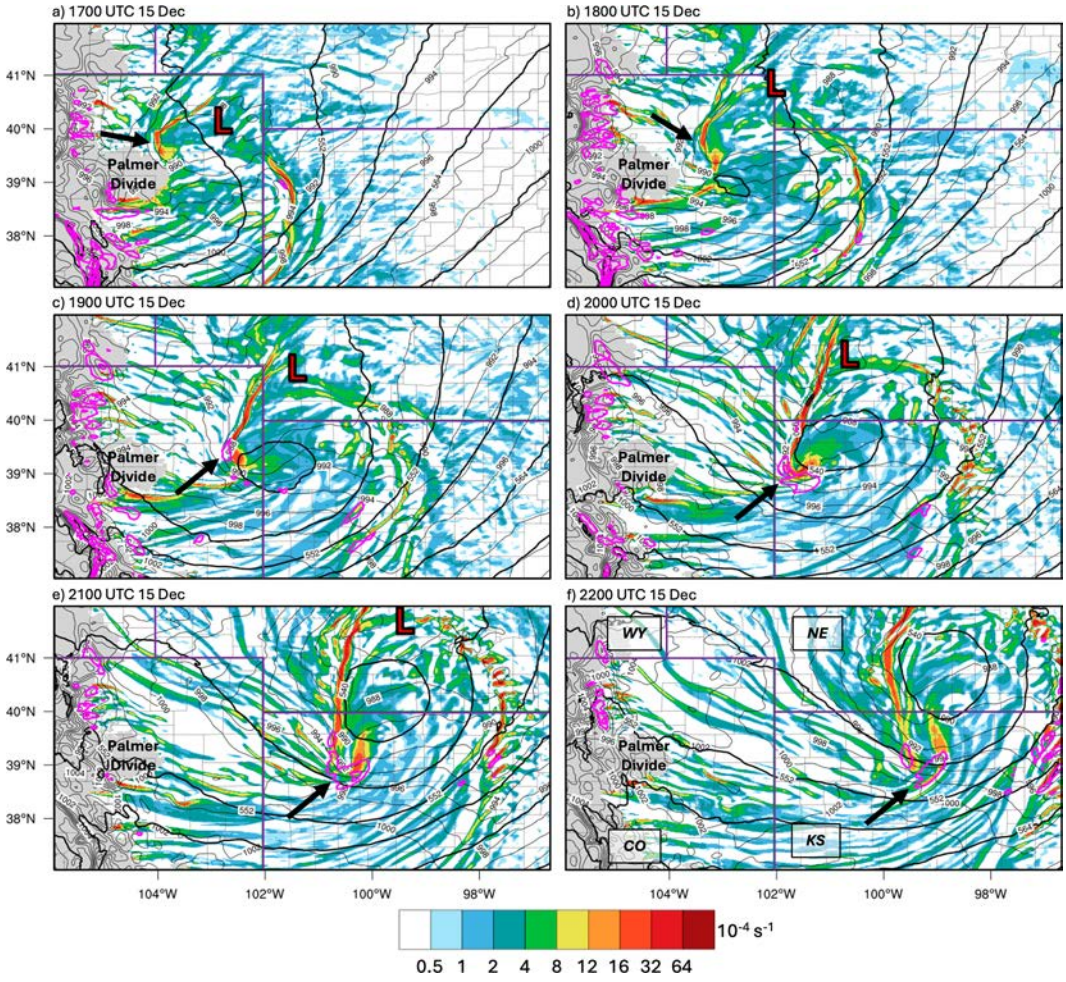

FIG. 12. ARW 500-hPa geopotential height (thick black contours every 6 dam), sea level pressure (thin black contours every 2 hPa), 800-hPa relative vorticity (shaded; 10^{-4} s^{-1}), and 80 m AGL wind speed (magenta contours every 5 m s^{-1} starting at 30 m s^{-1}) at (a) 1700 (5 h), (b) 1800 (6 h), (c) 1900 (7 h), (d) 2000 (8 h), (e) 2100 (9 h), and (f) 2200 UTC (10 h) 15 Dec 2021. The vorticity strip along the bent-back front and wind maximum at the tip of the bent-back front are labeled with a black arrow.

the decaying cloud head while other parcels remained in the drier air farther south of the cloud head. In all, the air within the near-surface wind maximum had its source from three separate airstreams that met near the southern tip of the bent-back front and the northwest region of the dry slot. For the westerly flow and bent-back airstreams that moved through the cloud head, acceleration of the winds occurred throughout their descent but at higher values while moving through the cloud head and into the higher horizontal pressure gradient region near the tip of the bent-back front (Fig. 16). The higher horizontal pressure gradient region developed as sea level pressure decreased near the southern tip of the bent-back front where the cyclonic vorticity strip rolled up and became more circular (Figs. 12c–e). Within this region, static stability in the PBL was reduced near the leading edge of the Arctic air mass at the eastern flank of the cloud head which likely aided in further descent of the high-momentum air from the top of the PBL to the surface (Fig. 13).

The possible role of II and CSI in acceleration of the wind speeds was likely secondary (Fig. 17). Some air parcels in the westerly flow and bent-back airstreams had absolute vorticity values below zero indicating the possibility of II, especially the westerly flow air parcels when they crossed the front range of the Rockies (Fig. 17a). The dry slot airstream for air parcel trajectories released at 2100 UTC indicated the possibility of CSI with moist PV values below zero (Fig. 17d). In the case of the conditions for II and CSI being satisfied, no clear wind speed accelerations were noted. The highest wind speed accelerations occurred later concurrent with the increase in the horizontal pressure gradient.

5. Discussion: Comparison of near-surface mesoscale wind maximum to sting jets

In the analysis above, it is shown that the extratropical cyclone and near-surface nonconvective mesoscale wind

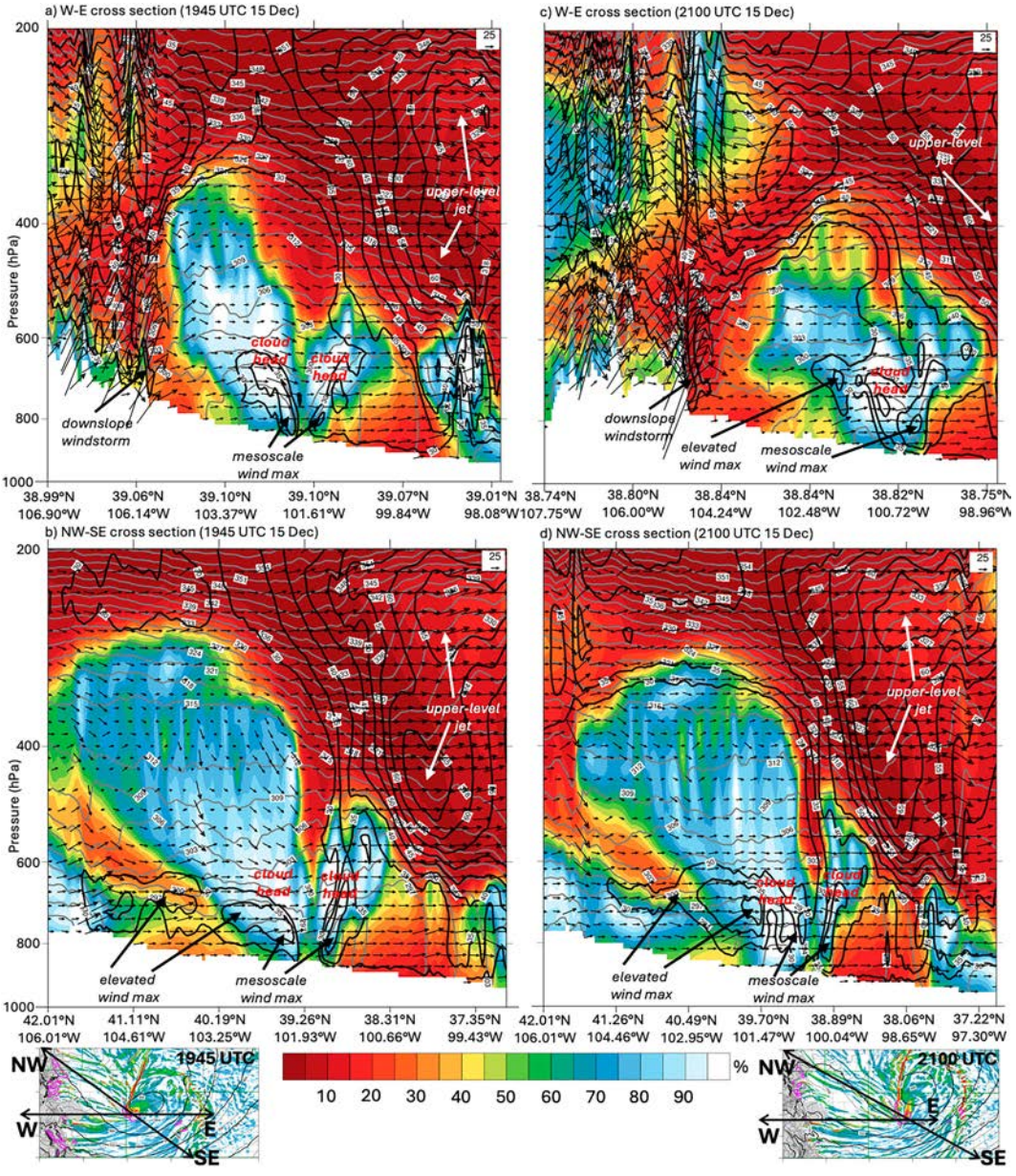

FIG. 13. ARW vertical cross sections of relative humidity (shaded; %), potential temperature (gray contours every 3 K), total wind speed (black contours every 5 m s^{-1} starting at 30 m s^{-1}), and circulation in the plane of the cross section (arrows; m s^{-1}) for west–east oriented sections at (a) 1945 and (c) 2100 UTC and northwest–southwest at (b) 1945 and (d) 2100 UTC 15 Dec 2021. The orientations of the cross sections at 1945 and 2100 UTC are shown in the insets at the bottom left and right of each column. The insets show the same fields as in Fig. 12. Key wind features are labeled with black and white arrows. The cloud head is labeled with red text.

maximum that contributed to the megafire in Kansas resembled an oceanic Shapiro–Keyser cyclone and sting jet, respectively. The aim of this subsection is to compare these structures to evaluate if the nonconvective mesoscale windstorm and megafire were linked to a true Shapiro–Keyser cyclone and sting jet or if the similarity was superficial.

Schultz and Keyser (2021) note that the defining features of a Shapiro–Keyser cyclone that distinguish it from a classic Norwegian model cyclone (Bjerknes 1919; Bjerknes and Solberg 1921, 1922) are the presence of a frontal fracture, bent-back front, frontal T-bone, and warm core seclusion (Shapiro and Keyser 1990, their Fig. 10.27). The frontal fracture develops in phase II of the Shapiro–Keyser cyclone model and is also apparent in the manual surface analysis at 2100 UTC (Fig. 6). The frontal fracture region is located on the north side of the cool air in the wake of the derecho and

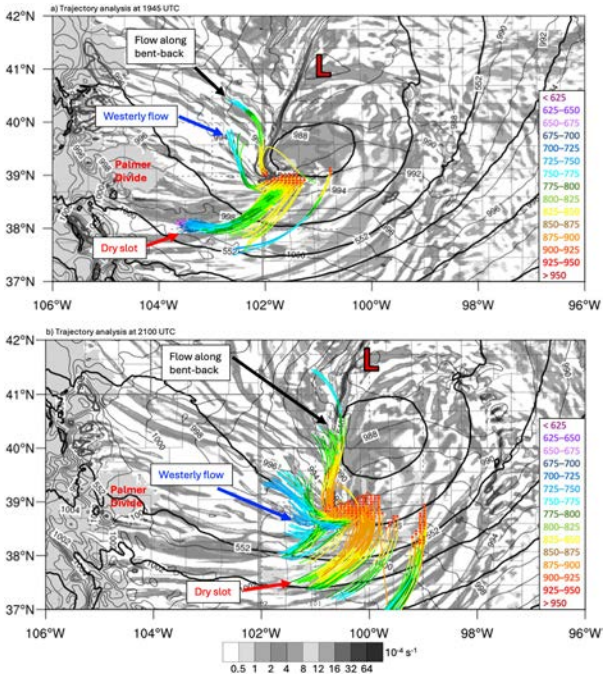

FIG. 14. ARW 500-hPa geopotential height (thick black contours every 6 dam), sea level pressure (thin black contours every 2 hPa), 800-hPa relative vorticity (shaded according to the grayscale in 10^{-4} s^{-1}), and 80 m AGL wind speed (dark gray contours every 5 m s^{-1} starting at 30 m s^{-1}) at (a) 1945 (7.75 h) and (b) 2100 UTC (9 h) 15 Dec 2021. Three-hour cyclone-relative air parcel backward trajectories starting at (a) 1945 UTC (7.75 h) at 825 hPa and (b) 2100 UTC (9 h) at 875 hPa are overlaid with starting locations marked by red-filled circles. The trajectories are colored by air parcel pressure (hPa) according to the key inset. Three separate airstreams were identified: flow along the bent-back front (labeled in black), westerly flow (blue), and dry slot flow (red). The location of the surface cyclone is marked by a red-filled black L.

cold front and just south of the warm front where the temperature gradient across the cold front weakens and the wind shift is not as well defined as farther south along the front. The frontal T bone represents the perpendicular orientation of the warm and cold fronts in the Shapiro–Keyser cyclone model. In the manual surface analysis, the orientation is not quite at a right angle at 2100 UTC but evolved to a right-angle orientation later on as the derecho and cold front surged northeastward (not shown).

In the Shapiro–Keyser cyclone model, the bent-back front forms as the warm front wraps cyclonically westward around the cyclone center in conjunction with the cold conveyor belt airstream. The bent-back front in the manual analysis and numerical simulation did not form in the same way, as it developed very early during cyclogenesis just southwest of the cyclone center and at the leading edge of an Arctic front (Figs. 6 and 10). The involvement of an Arctic front in formation of the bent-back front during cyclogenesis was similarly noted by Kelley et al. (2019, their Fig. 2) in the 25–26 December 2016 cyclone and windstorm. The cold conveyor belt was not seen in the 15 December 2021 cyclone based on the vertical cross-section wind analyses and air parcel trajectories (Figs. 13 and 14). Finally, the warm core seclusion forms during phase IV of the Shapiro–Keyser cyclone model as the bent-back front fully wraps around the cyclone center. A developing warm seclusion is apparent in the manual analysis and numerical simulation at 2100 UTC and later becomes isolated from the warm sector as the derecho and cold front surged northeastward (Figs. 6 and 10). In all, the extratropical cyclone on 15 December 2021 exhibited similar structures as a Shapiro–Keyser cyclone with the development of a frontal fracture, frontal T-bone, bent-back front, and warm core seclusion. However, the cyclone departs from the Shapiro–Keyser cyclone model in the pathway to developing each of these characteristics, perhaps most importantly, as it pertains to the mesoscale windstorm, with the nonconventional development of the bent-back front and the lack of an obvious cold conveyor belt.

As discussed in section 1b, the sting jet represents the descending airstream that reaches the top of the PBL ahead of the cold conveyor belt airstream and is capable of producing damaging winds at the surface (e.g., Clark and Gray 2018). The sting jet airstream originates where part of the ascending warm conveyor belt airstream turns cyclonically around the cyclone center and then descends within and near the tip of the cloud head and bent-back front (e.g., Schultz and Browning 2017). Although the cyclone on 15 December 2021 did not appear to have a well-developed cold conveyor belt airstream, the near-surface wind maximum was connected to a descending airstream in the cloud head that resembled the sting jet airstream in oceanic cyclones (Fig. 14). This airstream originated along the bent-back front, with several air parcel trajectories even showing cyclonic curvature somewhat similar to the airstream that connects to the warm conveyor belt in oceanic cyclones. Departing from the sting jet conceptual model, air in the near-surface wind maximum also had its origin in separate westerly flow and dry slot airstreams that originated at higher altitudes. A similar westerly flow airstream was noted by Kelley et al. (2019) and appears to be the air that moves through the mountain waves and downslope windstorm as it moves east across the Rockies and then as an elevated jet above the Arctic air mass behind the Arctic cold front (Fig. 13).

Mesoscale descent near the tip of the bent-back front in oceanic sting jet cases has been linked to frontolysis and the airstream accelerates as it descends into the higher horizontal pressure gradient region in the PBL near the surface (e.g., Schultz and Sienkiewicz 2013; Slater et al. 2017). Unlike oceanic sting jets, it appears that frontolysis is not a key mechanism that drives focused mesoscale descent near the tip of the bent-back front for the 15 December 2021 case (Fig. 18). Examination of Miller frontogenesis computed as in (1) shows a band of frontogenesis along the bent-back front at 1945 and 2100 UTC similar to the frontogenesis conceptual model presented by Schultz and Sienkiewicz (2013, their Fig. 6). However, frontolysis is not present near the tip of the bent-back front and above the near-surface wind maximum, which is somewhat consistent with the gradual descent of the sting jet airstream as it moved along the bent-back front and through the cloud head (Figs. 15a, 16a, and 18). Both the westerly flow

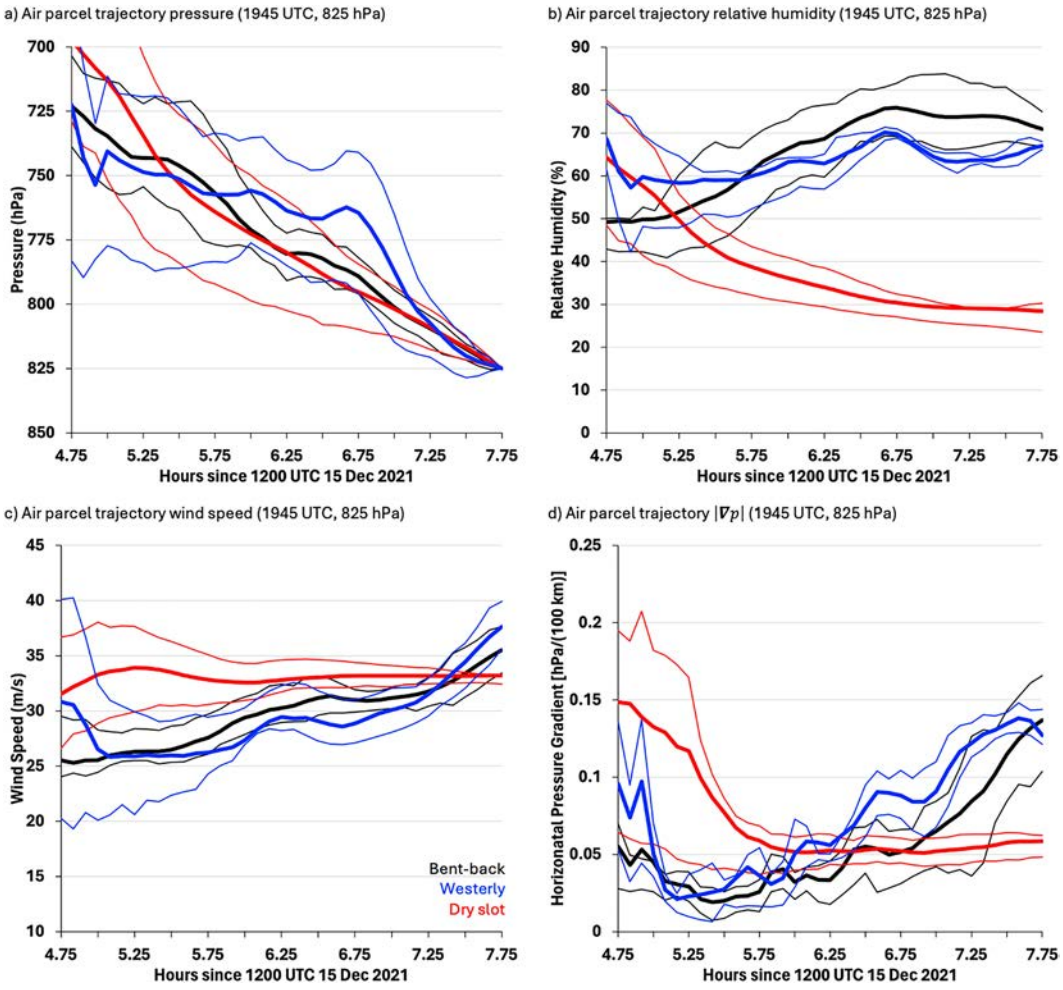

FIG. 15. Time series of (a) pressure (hPa), (b) relative humidity (%), wind speed (m s^{-1}), and (d) horizontal pressure gradient magnitude [hPa (100 km) $^{-1}$] for bent-back (black), westerly (blue), and dry slot (red) backward air parcel trajectories seeded at the 825-hPa pressure level at 1945 UTC 15 Dec 2021. The trajectory mean is plotted with a thick line and upper/lower quartiles with thin lines. Cyclone-relative trajectories are plotted in Fig. 14a.

and bent-back airstreams show acceleration as they descend through the cloud head and into the higher horizontal pressure gradient region near the top of the PBL, similar to previous studies of sting jets (e.g., Slater et al. 2017).

Finally, evaporative cooling in the cloud head above enhanced surface fluxes of heat and moisture helps to reduce the static stability of the PBL and allow the sting jet to reach the surface in oceanic cases (e.g., Browning et al. 2015; Schultz and Sienkiewicz 2013; Schultz and Browning 2017). While evaporative cooling likely occurred in the 15 December 2021 case as the cloud head dissipated, the reduced static stability in the PBL was likely linked to the well-mixed PBL near and just west of the Arctic cold front (Fig. 13). A well-mixed PBL was seen at and just west of the leading edge of the Arctic front of a similar case documented by Kelley et al. (2019). Perhaps, the presence of a well-mixed PBL near the Arctic front helps to compensate for the lack of a relatively warm ocean below and provides low static stability in the PBL for the strong winds to reach the surface.

6. Conclusions

This study presented a multiscale analysis and diagnosis of a nonconvective mesoscale windstorm in western and north-central Kansas on 15 December 2021. This event was part of two simultaneous extreme weather events associated with a deepening cyclone in the central Great Plains, where a derecho occurred along the cold front and the nonconvective mesoscale windstorm on the southwest side of the cyclone center. The windstorm downed power lines and triggered a megafire that led to two fatalities, numerous injuries, and killed hundreds of cattle. In all, the simultaneous extreme weather events on 15 December 2021 represented a billion-dollar weather disaster with significant socioeconomic impacts (NOAA 2024). We used observations, numerical model analyses and

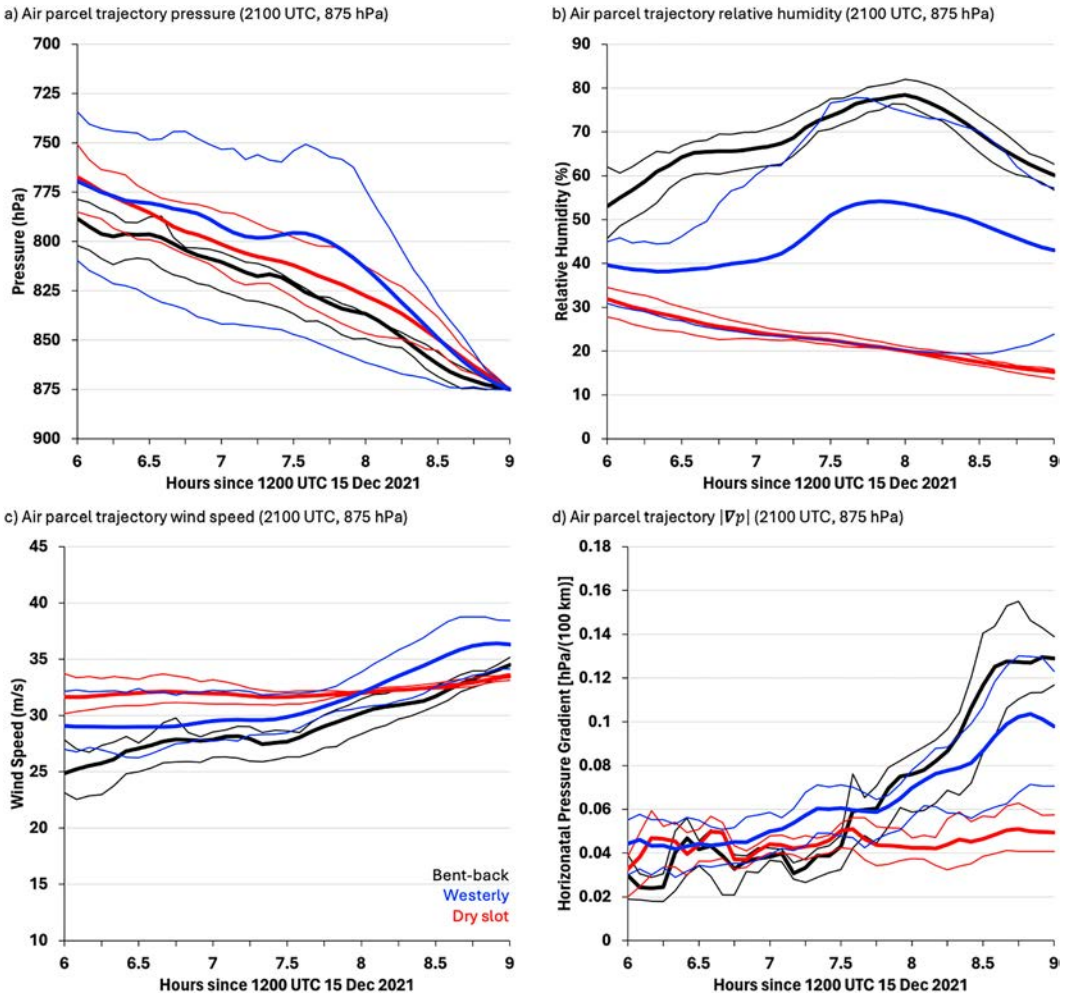

FIG. 16. As in Fig. 15, but for air parcels seeded at 875 hPa at 2100 UTC 15 Dec 2021. Cyclone-relative trajectories are plotted in Fig. 14b.

forecasts, and a convection-allowing numerical simulation using the ARW model to determine the physical mechanisms that led to the damaging winds on the southwest side of the cyclone center. The cyclone and nonconvective mesoscale wind maximum were then compared to the Shapiro–Keyser cyclone and sting jet conceptual models because of their structural similarity to those systems typically observed in ocean basins (Shapiro and Keyser 1990; Browning 2004; Gray et al. 2024).

The synoptic-scale flow pattern on 15 December 2021 was characterized by a progressive negatively tilted trough at 500 hPa and a deepening surface cyclone in the central Great Plains. The trough at 500 hPa was positioned in the Intermountain West on the morning of 15 December following two surface cyclogenesis events in the western and central North Pacific and subsequent downstream development beginning on 12 December. The dynamical linkages between wildfires in the western United States and upstream cyclogenesis in the North Pacific basin have been previously documented (e.g., Bosart et al. 2017), and we have extended these linkages to a wildfire outbreak in the plains that exhibited a similar flow pattern identified in megafire events (Lindley et al. 2019, 2023). The cyclone structure and evolution resembled the Shapiro–Keyser cyclone conceptual model (Shapiro and Keyser 1990; Schultz and Keyser 2021). The frontal fracture region, frontal T-bone, developing warm core seclusion, and bent-back front were all apparent, except that these features did not develop following the usual pathway in oceanic cyclones. The departure from the conceptual model occurred in particular for the bent-back front that developed in conjunction with an Arctic cold front, similar to the cyclone case documented by Kelley et al. (2019), rather than the typical westward extension of the warm front seen in oceanic Shapiro–Keyser cyclones.

While the near-surface wind maximum near the tip of the bent-back front exhibited many of the same characteristics of an oceanic sting jet, including an airstream along the bent-back front that descended and accelerated through the cloud head in a higher horizontal pressure gradient region near the tip of the bent-back front, it did not meet the exact definition

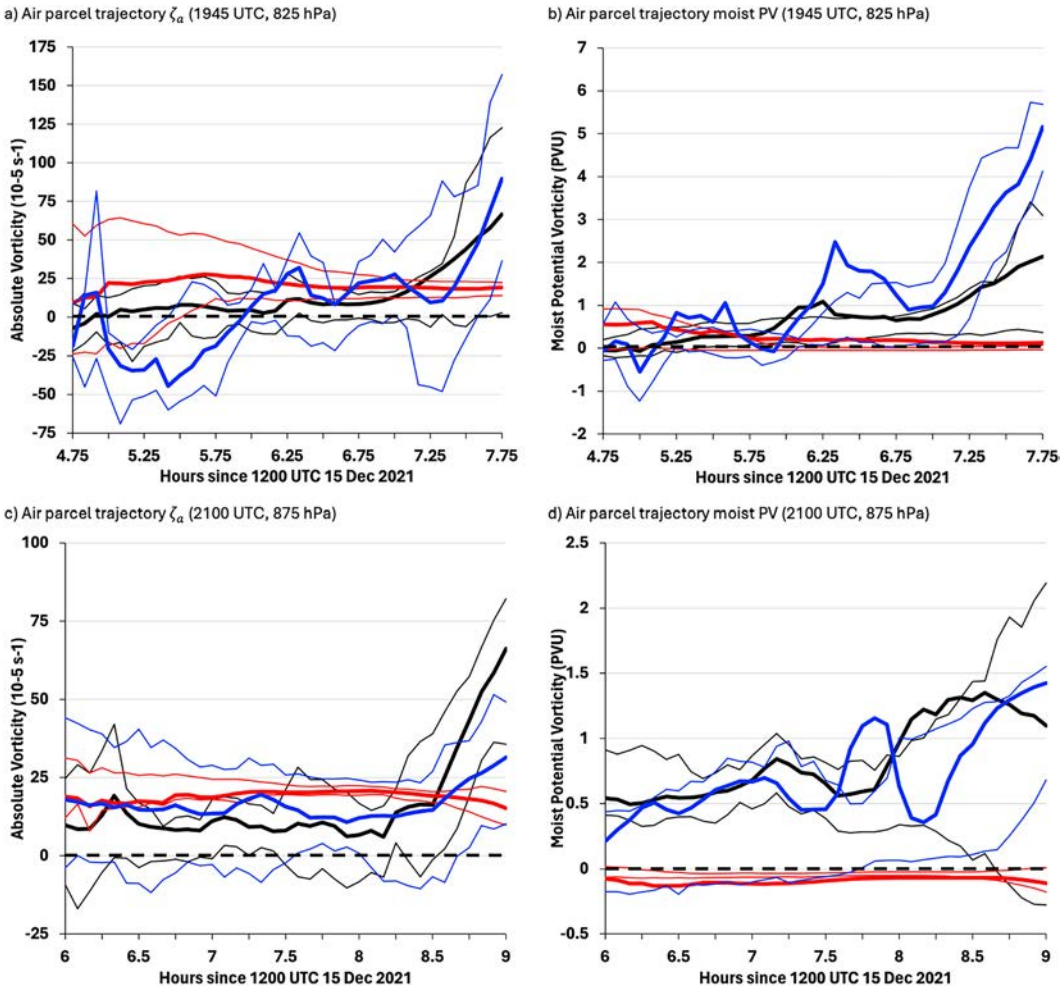

FIG. 17. Time series of (a) absolute vorticity (10^{-5} s^{-1}) and (b) moist PV (PVU) for bent-back (black), westerly (blue), and dry slot (red) backward air parcel trajectories seeded at the 825-hPa pressure level at 1945 UTC 15 Dec 2021. (c),(d) As in (a) and (b), but for trajectories seeded at the 875-hPa pressure level at 2100 UTC 15 Dec 2021. The trajectory mean is plotted with a thick line and upper/lower quartiles with thin lines. The zero line is marked by a black dashed line. Cyclone-relative trajectories are plotted in Fig. 14.

of a sting jet. Specifically, there were three descending airstreams—bent back, westerly flow, and dry slot—that contributed to the wind maximum rather than the single sting jet airstream (Clark and Gray 2018, Fig. 7). Additionally, frontolysis was not apparent near the tip of the bent-back front and therefore was likely not important in driving mesoscale descent (e.g., Schultz and Sienkiewicz 2013). Nonetheless, a wind maximum resembling a sting jet developed on the southwest of the cyclone center as the strip of cyclonic vorticity along the bent-back front rolled up on its southern end and the sea level pressure decreased. Similar evolution of vorticity has been documented along the bent-back front of cyclones in numerical simulations of idealized and real-data cases (e.g., Takayabu 1986; Reed et al. 1994; Galarneau and Weisman 2020). Concentrated vorticity maxima that develop in response to the rollup of vorticity along frontal zones can evolve into the cyclone center for developing systems in some cases (Wakimoto et al. 1995). As the sea level pressure decreased at the southern tip of the bent-back front, the near-surface horizontal pressure gradient increased, allowing for increasing wind speeds near the surface.

This study highlights the complex details of mesoscale features embedded within a favorable synoptic pattern that contributed to a nonconvective mesoscale windstorm and wildfire outbreak in the central Great Plains. Analysis of this case showed that the mechanisms driving the strongest winds had elements of the mechanisms documented in previous cases in the Great Plains (e.g., Kelley et al. 2019; Lindley et al. 2019) and with oceanic Shapiro–Keyser cyclones and sting jets (e.g., Clark and Gray 2018). In Gray et al.'s (2024) recent global climatology of sting jets using the "sting jet precursor" diagnostic, a relative maximum in genesis frequency was located in the Great Plains. We hypothesize that these events are likely similar to the 15 December 2021 case. While these events may not meet the exact definitions of the Shapiro–Keyser cyclone and sting jet conceptual models, they attain similar attributes

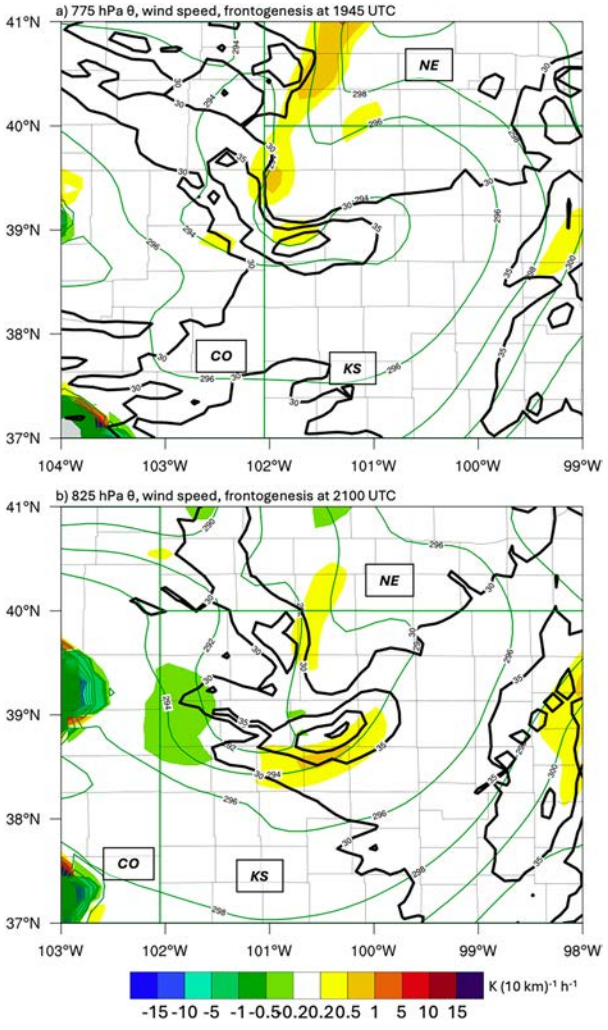

FIG. 18. ARW smoothed frontogenesis [shaded; K (10 km)$^{-1}$ h^{-1}], wind speed (black contours every 5 m s^{-1} starting at 30 m s^{-1}), and potential temperature (green contours every 2 K) at (a) 775 hPa at 1945 UTC (7.75 h) and (b) 825 hPa at 2100 UTC (9 h) 15 Dec 2021.

but by a different pathway compared to their oceanic counterparts. From an operational forecasting perspective, we argue that it is important to study and understand the complex mesoscale details that lead to the most intense winds and highest wildfire potential in an extratropical cyclone. These mesoscale details are often more difficult for numerical weather prediction models to forecast (e.g., Schultz and Browning 2017; Hewson and Neu 2015) and can contribute to uncertainties in the location and timing of the highest near-surface winds. Future research opportunities to increase understanding and improve prediction of nonconvective mesoscale windstorms and wildfires associated with extratropical cyclones in the Great Plains include 1) a systematic multiscale analysis over a large number of cases to assess the dynamic mechanisms driving the most intense winds and their relationship to features resembling Shapiro–Keyser cyclones and oceanic sting jets and 2) predictability studies to determine numerical weather prediction model biases and failure modes in forecasting the timing and location of the mesoscale region of most intense winds.

Acknowledgments. This study benefited from conversations with David Schultz and Kim Hoogewind. Adam Clark and Pam Heinselman kindly provided comments on the manuscript. We thank three anonymous reviewers for their helpful comments and constructive criticisms. Partial support was provided by National Science Foundation Grant 2039388 and NOAA/Office of Oceanic and Atmospheric Research under NOAA–University of Oklahoma Cooperative Agreement NA21OAR4320204, U.S. Department of Commerce. The ARW simulation was generated using the local computing cluster at the NOAA/OAR National Severe Storms Laboratory.

Data availability statement. The numerical simulation was generated using the WRF-ARW Model (https://doi.org/10.5065/D6MK6B4K). The ERA5 was downloaded from https://doi.org/10.24381/cds.adbb2d47, and its availability is subject to the policies of ECMWF. All other datasets are freely available, with GFS analysis and surface observations available at NOAA NCEI, HREFv3 imagery from SPC (https://www.spc.noaa.gov/exper/href/), drought information from https://droughtmonitor.unl.edu/, and satellite imagery from the CIMSS satellite blog (https://cimss.ssec.wisc.edu/satellite-blog/) and the NWS at Wichita (https://www.weather.gov/ict/event_2021Dec15thWindFireSVR). Air parcel trajectories were computed using Read/Interpolate/Plot, version 4.7 (https://www2.mmm.ucar.edu/wrf/users/docs/ripug.htm), and all other calculations were made using NCAR Command Language, version 6.6.2 (https://www.ncl.ucar.edu/).

REFERENCES

Abatzoglou, J. T., and C. A. Kolden, 2013: Relationships between climate and macroscale area burned in the western United States. *Int. J. Wildland Fire*, **22**, 1003–1020, https://doi.org/10.1071/WF13019.

Ashley, W. S., and A. W. Black, 2008: Fatalities associated with nonconvective high-wind events in the United States. *J. Appl. Meteor. Climatol.*, **47**, 717–725, https://doi.org/10.1175/2007JAMC1689.1.

Baker, L. H., S. L. Gray, and P. A. Clark, 2014: Idealised simulations of sting-jet cyclones. *Quart. J. Roy. Meteor. Soc.*, **140**, 96–110, https://doi.org/10.1002/qj.2131.

Bjerknes, J., 1919: On the structure of moving cyclones. *Mon. Wea. Rev.*, **47**, 95–99, https://doi.org/10.1175/1520-0493(1919)47%3C95:OTSOMC%3E2.0.CO;2.

——, and H. S. Solberg, 1921: Meteorological conditions for the formation of rain. *Geofys. Publ.*, **2**, 1–60.

——, and ——, 1922: Life cycle of cyclones and the polar front theory of atmospheric circulation. *Geofys. Publ.*, **3**, 3–18.

Bosart, L. F., B. J. Moore, J. M. Cordeira, and H. M. Archambault, 2017: Interactions of North Pacific tropical, midlatitude, and polar disturbances resulting in linked extreme weather events over

North America in October 2007. *Mon. Wea. Rev.*, **145**, 1245–1273, https://doi.org/10.1175/MWR-D-16-0230.1.

Brâncuş, M., D. M. Schultz, B. Antonescu, C. Dearden, and S. Ştefan, 2019: Origin of strong winds in an explosive Mediterranean extratropical cyclone. *Mon. Wea. Rev.*, **147**, 3649–3671, https://doi.org/10.1175/MWR-D-19-0009.1.

Browning, K. A., 2004: The sting at the end of the tail: Damaging winds associated with extratropical cyclones. *Quart. J. Roy. Meteor. Soc.*, **130**, 375–399, https://doi.org/10.1256/qj.02.143.

——, D. J. Smart, M. R. Clark, and A. J. Illingworth, 2015: The role of evaporating showers in the transfer of sting-jet momentum to the surface. *Quart. J. Roy. Meteor. Soc.*, **141**, 2956–2971, https://doi.org/10.1002/qj.2581.

Burroughs, L. D., 1987: Development of forecast guidance for Santa Ana conditions. *Natl. Wea. Dig.*, **12**, 4–11.

Carlson, T. N., 1980: Airflow through midlatitude cyclones and the comma cloud pattern. *Mon. Wea. Rev.*, **108**, 1498–1509, https://doi.org/10.1175/1520-0493(1980)108<1498:ATMCAT>2.0.CO;2.

Clark, P. A., and S. L. Gray, 2018: Sting jets in extratropical cyclones: A review. *Quart. J. Roy. Meteor. Soc.*, **144**, 943–969, https://doi.org/10.1002/qj.3267.

——, K. A. Browning, and C. Wang, 2005: The sting at the end of the tail: Model diagnostics of fine-scale three-dimensional structure of the cloud head. *Quart. J. Roy. Meteor. Soc.*, **131**, 2263–2292, https://doi.org/10.1256/qj.04.36.

Corfidi, S. F., M. C. Coniglio, A. E. Cohen, and C. M. Mead, 2016: A proposed revision to the definition of "derecho". *Bull. Amer. Meteor. Soc.*, **97**, 935–949, https://doi.org/10.1175/BAMS-D-14-00254.1.

Donovan, V. M., C. L. Wonkka, and D. Twidwell, 2017: Surging wildfire activity in a grassland biome. *Geophys. Res. Lett.*, **44**, 5986–5993, https://doi.org/10.1002/2017GL072901.

Dudhia, J., 1989: Numerical study of convection observed during the Winter Monsoon Experiment using a mesoscale two-dimensional model. *J. Atmos. Sci.*, **46**, 3077–3107, https://doi.org/10.1175/1520-0469(1989)046<3077:NSOCOD>2.0.CO;2.

Durran, D. R., 1990: Mountain waves and downslope winds. *Atmospheric Processes over Complex Terrain*, W. Blumen, Ed., Amer. Meteor. Soc., 59–81.

Earl, N., S. Dorling, M. Starks, and R. Finch, 2017: Subsynoptic-scale features associated with extreme surface gusts in UK extratropical cyclone events. *Geophys. Res. Lett.*, **44**, 3932–3940, https://doi.org/10.1002/2017GL073124.

Fujita, T. T., 1981: Tornadoes and downbursts in the context of generalized planetary scales. *J. Atmos. Sci.*, **38**, 1511–1534, https://doi.org/10.1175/1520-0469(1981)038<1511:TADITC>2.0.CO;2.

Galarneau, T. J., Jr., and M. L. Weisman, 2020: A comparison of the vorticity dynamics governing the oceanic bomb cyclone of 4–5 January 1989 and the super derecho of 8 May 2009. *J. Atmos. Sci.*, **77**, 3081–3103, https://doi.org/10.1175/JAS-D-20-0179.1.

——, and X. Zeng, 2020: The Hurricane Harvey (2017) Texas rainstorm: Synoptic analysis and sensitivity to soil moisture. *Mon. Wea. Rev.*, **148**, 2479–2502, https://doi.org/10.1175/MWR-D-19-0308.1.

Gray, S. L., O. Martínez-Alvarado, L. H. Baker, and P. A. Clark, 2011: Conditional symmetric instability in sting-jet storms. *Quart. J. Roy. Meteor. Soc.*, **137**, 1482–1500, https://doi.org/10.1002/qj.859.

——, A. Volonte, O. Martinez-Alvarado, and B. J. Harvey, 2024: A global climatology of sting-jet extratropical cyclones. *Wea. Climate Dyn.*, **5**, 1523–1544, https://doi.org/10.5194/wcd-5-1523-2024.

Grønås, S., 1995: The seclusion intensification of the New Year's day storm 1992. *Tellus*, **47A**, 733–746, https://doi.org/10.3402/tellusa.v47i5.11571.

Hart, N. C. G., S. L. Gray, and P. A. Clark, 2017: Sting-jet windstorms over the North Atlantic: Climatology and contribution to extreme wind risk. *J. Climate*, **30**, 5455–5471, https://doi.org/10.1175/JCLI-D-16-0791.1.

Hatzaki, M., and Coauthors, 2023: MedCyclones: Working together toward understanding Mediterranean cyclones. *Bull. Amer. Meteor. Soc.*, **104**, E480–E487, https://doi.org/10.1175/BAMS-D-22-0280.1.

Heinselman, P. L., and Coauthors, 2024: Warn-on-Forecast System: From vision to reality. *Wea. Forecasting*, **39**, 75–95, https://doi.org/10.1175/WAF-D-23-0147.1.

Hersbach, H., and Coauthors, 2020: The ERA5 global reanalysis. *Quart. J. Roy. Meteor. Soc.*, **146**, 1999–2049, https://doi.org/10.1002/qj.3803.

Hewson, T. D., and U. Neu, 2015: Cyclones, windstorms and the IMILAST project. *Tellus*, **67A**, 27128, https://doi.org/10.3402/tellusa.v67.27128.

Hong, S.-Y., Y. Noh, and J. Dudhia, 2006: A new vertical diffusion package with an explicit treatment of entrainment processes. *Mon. Wea. Rev.*, **134**, 2318–2341, https://doi.org/10.1175/MWR3199.1.

Johns, R. H., and W. D. Hirt, 1987: Derechos: Widespread convectively induced windstorms. *Wea. Forecasting*, **2**, 32–49, https://doi.org/10.1175/1520-0434(1987)002<0032:DWCIW>2.0.CO;2.

Kansas Forest Service, 2021: Kansas forest health highlights 2021. Kansas Forest Service, 19 pp., https://www.kansasforests.org/forest_health/health_docs/FHH%202021.pdf.

Kelley, J. D., D. M. Schultz, R. S. Schumacher, and D. R. Durran, 2019: Can Mountain waves contribute to damaging winds far away from the lee slope? *Wea. Forecasting*, **34**, 2045–2065, https://doi.org/10.1175/WAF-D-18-0207.1.

Kenyon, J. S., D. Keyser, L. F. Bosart, and M. S. Evans, 2020: The motion of mesoscale snowbands in northeast U.S. winter storms. *Wea. Forecasting*, **35**, 83–105, https://doi.org/10.1175/WAF-D-19-0038.1.

Keyser, D., M. J. Reeder, and R. J. Reed, 1988: A generalization of Petterssen's frontogenesis function and its relation to the forcing of vertical motion. *Mon. Wea. Rev.*, **116**, 762–781, https://doi.org/10.1175/1520-0493(1988)116<0762:AGOPFF>2.0.CO;2.

Kitabatake, N., 2008: Extratropical transition of tropical cyclones in the western North Pacific: Their frontal evolution. *Mon. Wea. Rev.*, **136**, 2066–2090, https://doi.org/10.1175/2007MWR1958.1.

Kite, A., 2021: 'Ball of rolling fire and smoke': Wildfires rip through north-central Kansas. Kansas Reflector, accessed 10 June 2024, https://kansasreflector.com/2021/12/20/ball-of-rolling-fire-and-smoke-wildfires-rip-through-north-central-kansas/.

Knox, J. A., J. D. Frye, J. D. Durkee, and C. M. Fuhrmann, 2011: Non-convective high winds associated with extratropical cyclones. *Geogr. Compass*, **5**, 63–89, https://doi.org/10.1111/j.1749-8198.2010.00395.x.

Lindley, T. T., and Coauthors, 2014: Southern Great Plains wildfire outbreaks. *Electron. J. Severe Storms Meteor.*, **9**, https://ejssm.org/archives/wp-content/uploads/2021/09/vol9-2.pdf.

——, B. R. Bowers, G. P. Murdoch, B. R. Smith, and C. M. Gitro, 2017: Analyses of fire-effective low-level thermal ridges on the Southern Great Plains. *J. Oper. Meteor.*, **5**, 146–160, https://doi.org/10.15191/nwajom.2017.0512.

——, D. A. Speheger, M. A. Day, G. P. Murdoch, B. R. Smith, N. J. Nauslar, and D. C. Daily, 2019: Megafires on the Southern Great Plains. *J. Oper. Meteor.*, **7**, 164–179, https://doi.org/10.15191/nwajom.2019.0712.

——, A. B. Zwink, R. R. Barnes, G. P. Murdoch, B. C. Ancell, P. C. Burke, and P. S. Skinner, 2023: Preliminary use of convection-allowing models in fire weather. *J. Oper. Meteor.*, **11**, 72–81, https://doi.org/10.15191/nwajom.2023.1106.

Mansell, E. R., C. L. Ziegler, and E. C. Bruning, 2010: Simulated electrification of a small thunderstorm with two-moment bulk microphysics. *J. Atmos. Sci.*, **67**, 171–194, https://doi.org/10.1175/2009JAS2965.1.

Martínez-Alvarado, O., S. L. Gray, J. L. Catto, and P. A. Clark, 2012: Sting jets in intense winter North-Atlantic windstorms. *Environ. Res. Lett.*, **7**, 024014, https://doi.org/10.1088/1748-9326/7/2/024014.

Mass, C., and B. Dotson, 2010: Major extratropical cyclones of the Northwest United States: Historical review, climatology, and synoptic environment. *Mon. Wea. Rev.*, **138**, 2499–2527, https://doi.org/10.1175/2010MWR3213.1.

Miller, J. E., 1948: On the concept of frontogenesis. *J. Meteor.*, **5**, 169–171, https://doi.org/10.1175/1520-0469(1948)005<0169:OTCOF>2.0.CO;2.

NOAA, 2024: NOAA/NCEI storm events database version 3.1. NOAA, accessed 3 September 2022, https://www.ncdc.noaa.gov/stormevents/.

NWCG, 2022: Fire Behavior Field Reference Guide, PMS 437. National Wildfire Coordinating Group, accessed 16 March 2023, https://www.nwcg.gov/publications/pms437/fire-behavior-field-reference-guide-pms-437.

Petterssen, S., 1936: Contribution to the theory of frontogenesis. *Geofys. Publ.*, **11**, 1–27.

Pyne, S. J., 2017: The Great Plains: A Fire Survey. The University of Arizona Press, 217 pp.

Reed, R. J., Y.-H. Kuo, and S. Low-Nam, 1994: An adiabatic simulation of the ERICA IOP 4 storm: An example of quasi-ideal frontal cyclone development. *Mon. Wea. Rev.*, **122**, 2688–2708, https://doi.org/10.1175/1520-0493(1994)122<2688:AASOTE>2.0.CO;2.

Ruppert, J. H., Jr., and L. F. Bosart, 2014: A case study of the interaction of a mesoscale gravity wave with a mesoscale convective system. *Mon. Wea. Rev.*, **142**, 1403–1429, https://doi.org/10.1175/MWR-D-13-00274.1.

Sanders, F., and J. R. Gyakum, 1980: Synoptic-dynamic climatology of the "bomb". *Mon. Wea. Rev.*, **108**, 1589–1606, https://doi.org/10.1175/1520-0493(1980)108<1589:SDCOT>2.0.CO;2.

Schultz, D. M., and J. M. Sienkiewicz, 2013: Using frontogenesis to identify sting jets in extratropical cyclones. *Wea. Forecasting*, **28**, 603–613, https://doi.org/10.1175/WAF-D-12-00126.1.

——, and K. A. Browning, 2017: What is a sting jet? *Weather*, **72**, 63–66, https://doi.org/10.1002/wea.2795.

——, and D. Keyser, 2021: Antecedents for the Shapiro-Keyser cyclone model in the Bergen school literature. *Bull. Amer. Meteor. Soc.*, **102**, E383–E398, https://doi.org/10.1175/BAMS-D-20-0078.1.

——, ——, and L. F. Bosart, 1998: The effect of large-scale flow on low-level frontal structure and evolution in midlatitude cyclones. *Mon. Wea. Rev.*, **126**, 1767–1791, https://doi.org/10.1175/1520-0493(1998)126<1767:TEOLSF>2.0.CO;2.

Shapiro, M. A., and D. Keyser, 1990: Fronts, jet streams, and the tropopause. *Extratropical Cyclones: The Erik Palmén Memorial Volume*, C. W. Newton and E. O. Holopainen, Eds., Amer. Meteor. Soc., 167–191.

Skamarock, W. C., and Coauthors, 2008: A description of the Advanced Research WRF version 3. NCAR Tech. Note NCAR/TN-475+STR, 113 pp., https://doi.org/10.5065/D68S4MVH.

Slater, T. P., D. M. Schultz, and G. Vaughan, 2015: Acceleration of near-surface strong winds in a dry, idealised extratropical cyclone. *Quart. J. Roy. Meteor. Soc.*, **141**, 1004–1016, https://doi.org/10.1002/qj.2417.

——, ——, and ——, 2017: Near-surface strong winds in a marine extratropical cyclone: Acceleration of the winds and the importance of surface fluxes. *Quart. J. Roy. Meteor. Soc.*, **143**, 321–332, https://doi.org/10.1002/qj.2924.

Smart, D. J., and K. A. Browning, 2014: Attribution of strong winds to a cold conveyor belt and sting jet. *Quart. J. Roy. Meteor. Soc.*, **140**, 595–610, https://doi.org/10.1002/qj.2162.

Smirnova, T. G., J. M. Brown, S. G. Benjamin, and J. S. Kenyon, 2016: Modifications to the Rapid Update Cycle Land Surface Model (RUC LSM) available in the Weather Research and Forecasting (WRF) Model. *Mon. Wea. Rev.*, **144**, 1851–1865, https://doi.org/10.1175/MWR-D-15-0198.1.

Smith, C. M., B. J. Hatchett, and M. L. Kaplan, 2018: Characteristics of sundowner winds near Santa Barbara, California, from a dynamically downscaled climatology: Environment and effects near the surface. *J. Appl. Meteor. Climatol.*, **57**, 589–606, https://doi.org/10.1175/JAMC-D-17-0162.1.

Sommers, W. T., 1978: LFM forecast variables related to Santa Ana wind occurrences. *Mon. Wea. Rev.*, **106**, 1307–1316, https://doi.org/10.1175/1520-0493(1978)106<1307:LFVRTS>2.0.CO;2.

State of Kansas, 2023: Governor's Wildfire Task Force. Final Rep., 42 pp., https://www.kansasforests.org/fire_management/Wildfire-Task-Force-Report_FINAL.pdf.

Stuivenvolt-Allen, J., and S.-Y. Wang, 2023: North American fire weather catalyzed by the extratropical transition of tropical cyclones. *Climate Dyn.*, **61**, 65–78, https://doi.org/10.1007/s00382-022-06561-1.

——, ——, M. D. LaPlante, and J.-H. Yoon, 2021: Three western Pacific typhoons strengthened fire weather in the recent Northwest U.S. conflagration. *Geophys. Res. Lett.*, **48**, e2020GL091430, https://doi.org/10.1029/2020GL091430.

Takayabu, I., 1986: Roles of the horizontal advection on the formation of surface fronts and on the occlusion of a cyclone developing in the baroclinic westerly jet. *J. Meteor. Soc. Japan*, **64**, 329–345, https://doi.org/10.2151/jmsj1965.64.3_329.

Wakimoto, R. M., N. T. Atkins, and C. Liu, 1995: Observations of the early evolution of an explosive oceanic cyclone during ERICA IOP 5. Part II: Airborne Doppler analysis of the mesoscale circulation and frontal structure. *Mon. Wea. Rev.*, **123**, 1311–1327, https://doi.org/10.1175/1520-0493(1995)123<1311:OOTEEO>2.0.CO;2.

WSEC, 2006: A recommendation for an Enhanced Fujita scale (EF-scale). Texas Tech University Wind Science and Engineering Center Rep., 111 pp., https://www.depts.ttu.edu/nwi/Pubs/FScale/EFScale.pdf.

Zscheischler, J., and Coauthors, 2020: A typology of compound weather and climate events. *Nat. Rev. Earth Environ.*, **1**, 333–347, https://doi.org/10.1038/s43017-020-0060-z.